Journal of Hydrology 572 (2019) 364–379

Contents lists available at ScienceDirect

Journal of Hydrology

journal homepage: www.elsevier.com/locate/jhydrol

Numerical investigation of the combined effect of forced and free thermal convection in synthetic groundwater basins

Márk Szijártó[a,*], Attila Galsa[a], Ádám Tóth[b], Judit Mádl-Szőnyi[b]

[a] Department of Geophysics and Space Science, ELTE Eötvös Loránd University, Budapest, Hungary
[b] Department of Physical and Applied Geology, József & Erzsébet Tóth Endowed Hydrogeology Chair, ELTE Eötvös Loránd University, Budapest, Hungary

ARTICLE INFO

This manuscript was handled by C. Corradini, Editor-in-Chief, with the assistance of Okke Batelaan, Associate Editor

Keywords:
Topography-driven groundwater flow
Thermal buoyancy
Forced and free thermal convection
Finite element numerical modeling
Heat transport

ABSTRACT

The theoretical examination of the combined effect of water table configuration and heat transfer is relevant to improve understanding of deep groundwater systems, not only in siliciclastic sedimentary basins, but also in fractured rocks or karstified carbonates. Numerical model calculations have been carried out to investigate the interaction of topography-driven forced and buoyancy-driven free thermal convection in a synthetic, two-dimensional model. Effects of numerous model parameters were systematically studied in order to examine their influence on the Darcy flux, the temperature and the hydraulic head field. It was established that higher geothermal gradients and greater model depths facilitate the evolution of time-dependent free thermal convection in agreement with changes of the thermal Rayleigh number and the modified Péclet number. However, increasing water table slope and anisotropy coefficient favor the formation of stationary forced thermal convection. Free thermal convection mainly affects the deeper part of the midline and the discharge zone of the synthetic model. In the examined model basins, the position of the maximum hydraulic head is located within the bottom thermal boundary layer near the recharge zone. This divergent stagnation point underlies a local downwelling zone characterized by underpressure. These simulations draw attention to the importance of understanding the combined effect of forced and free thermal convection in sedimentary basins regarding regional groundwater flow patterns, and temperature distributions.

1. Introduction

On the basis of field observations and analytical considerations, in the 19th century, the water table configuration was considered as the unique driving force of regional groundwater flow (e.g. Hubbert, 1940; Tóth, 1962, 1963) which can be relevant in the case of small drainage basins with limited depth (1–2 km) (e.g. Zhang et al., 2018; Jiang et al., 2018). As a first approximation, the water table configuration is controlled by the topography, hereinafter this kind of flow is referred to as topography-driven groundwater flow (Person et al., 1996). Since publication of these seminal papers on groundwater flow in sedimentary basins, it has been perceived that groundwater motion can also be induced by other geological processes, including sedimentary compaction (e.g. Sharp, 1976; Cathles and Smith, 1983; Bethke, 1985; Harrison and Summa, 1991), tectonic compression (e.g. Oliver, 1986; Ge and Garven, 1989; Tóth and Almási, 2001), density change by chemical composition (e.g. Voss and Souza, 1987; Simmons et al., 1999; van Dam et al., 2009; Voss et al., 2010), or heat transfer (e.g. Horton and Rogers, 1945; Bredehoeft and Papadopulos, 1965; Rabinowicz et al., 1998; Shojae Ghias et al., 2017). Beyond these driving forces on basin-scale flow systems, groundwater flow is also influenced by other physical parameters, for instance, model geometry (e.g. Freeze and Witherspoon, 1966, 1967, 1968), permeability or hydraulic conductivity (e.g. Jiang et al., 2009; Jiang et al., 2010a) and anisotropy (e.g. Winter and Pfannkuch, 1984; Galsa, 1997; Cardenas and Jiang, 2010; Jiang et al., 2010b; Wang et al., 2011).

Focusing on the effects of pure heat transfer, Lapwood (1948) pointed out that in two-dimensional, horizontally infinite, homogeneous and isotropic model domains with a permeable surface, no free thermal convection takes place due to buoyancy forces when the thermal Rayleigh number (Ra) is lower than the critical value, $Ra < Ra_{cr} = 27.1$. At values slightly above the critical Rayleigh number, stationary, two-dimensional thermal convection forms in a porous layer (Elder, 1967). As Ra increases, the form of the thermal convection changes from steady-state to time-dependent periodic, then quasi-periodic states. Numerical investigations suggested the existence of free thermal convection in sedimentary basins as an explanation for high surface heat flux (Straus and Schubert, 1977). The high geothermal

* Corresponding author.
E-mail address: mark.szijarto@ttk.elte.hu (M. Szijártó).

https://doi.org/10.1016/j.jhydrol.2019.03.003
Received 30 July 2018; Received in revised form 20 February 2019; Accepted 21 February 2019
Available online 06 March 2019

gradient from borehole measurements in the sedimentary basin of Tiszakécske (Great Hungarian Plain), for example, was explained as an upwelling part of a thermal convection cell by Lenkey (1993) without taking into consideration topography-driven groundwater flow.

In their pioneering study, Domenico and Palciauskas (1973) were the first who investigated the relationship between topography-driven groundwater flow and heat transfer theoretically. They distinguished between two types of thermal convection. They focused on only forced convection which may be taken to mean that flow is driven by an external force, e.g. by topography variation of the water table, while the effect of thermal buoyancy was neglected. Similarly, An et al. (2015) investigated temperature distribution in a simple and in a complex basin model of Tóth (1963), in which groundwater flow was induced purely by water table variation, that is, they studied the effect of forced convection.

The interaction of topography-driven forced and buoyancy-driven free thermal convection on the surface heat flux was analyzed in a synthetic model by Smith and Chapman (1983) only in steady-state groundwater flow. Recognizing the importance of time-dependent free thermal convection, Cserepes and Lenkey (2004) completed a comprehensive systematic study to map the groundwater flow pattern as functions of the slope of the topography and the thermal Rayleigh number. The increasing effect of topography-driven forced convection was investigated in a conceptual model at low water table slope and low Rayleigh number by Yang et al. (2010). They concluded that when the Darcy flux generated by free thermal convection exceeds the Darcy flux from forced convection, a mixed free and forced convection evolves in the system.

The effect of forced and free thermal convection was investigated numerically by Raffensperger and Vlassopoulos (1999) in a sedimentary basin, where the dominance of steady-state groundwater flow was noticed because of the low Rayleigh numbers ($Ra < 100$). For the Rheingraben, Clauser and Villinger (1990) presented a complete case study, including forced and free thermal convection by two-dimensional numerical simulations. Based on regional-scale numerical simulations and field observations, Lopez et al. (2016) proved the existence of time-dependent forced and free (mixed) thermal convection in a heterogeneous siliciclastic formation of the Lake Chad Basin ($Ra < 380$). In this case the blocks of the basin were separated by faults which strongly influencing the location, the path and the intensity of thermal convection similar to previous studies by Yang et al. (2004, 2006).

In the deeper parts of the carbonate aquifers, the enhanced temperature gradient observations can suggest the presence of forced convection (e.g. Pasquale et al., 2013). Numerical simulations have been carried out to compare the temperature distribution caused by thermal convection with observed temperature-depth profiles and elucidate temperature anomalies and flow patterns in the deep carbonate platform of Luttelgeest in the Netherlands (Lipsey et al., 2016). The groundwater flow system in confined and unconfined carbonate regions has also been studied (e.g. Goldscheider et al., 2010; Mádl-Szőnyi and Tóth, 2015; Mádl-Szőnyi et al., 2017), where the importance of free thermal convection was mentioned. Semi-synthetic numerical simulations were carried out on a basin-scale model by Havril et al. (2016) to qualitatively understand the evolving hydrodynamic flow system of the Buda Thermal Karst in Hungary. According to this study, in early evolutionary stages the groundwater flow system was dominated by free thermal convection ($Ra < 360$), which was partially overwritten by topography-driven flow after tectonic uplift of the Buda block. However the combined effect of the topography-driven external force and the thermal buoyancy force has not been investigated comprehensively.

Based on these preliminary considerations, the main goal of the present study was the systematic numerical investigation of the combined effects of topography-driven forced and buoyancy-driven free thermal convection. A simple two-dimensional, homogeneous isotropic model (Tóth, 1962) was used as a base model in order to focus on the physics of the phenomenon. The basic questions were as follows: (i) what is the pattern of the interaction of two driving forces in the model basin; (ii) how does this interaction influence the flow, the temperature and the hydraulic head inducing over- and underpressure, stagnation point 'skipping', etc.

Over the course of this theoretical experiment, four model parameters were systematically altered: (1) the temperature difference between the bottom and the surface of the model, (2) the model depth, (3) the slope of the water table and (4) the anisotropy of the hydraulic conductivity. For the simulated scenarios, changes in the non-dimensional Rayleigh and modified Péclet number were also followed to study the transition between stationary forced and time-dependent free thermal convection.

2. Model description and definition of monitoring parameters

In order to investigate the combined effect of regional-scale forced and free thermal convection in a synthetic groundwater flow basin, the equations of continuity, Darcy's Law and heat transfer (Bear and Verruijt, 1987; Nield and Bejan, 2017) were coupled and solved numerically, respectively given by

$$\varphi\frac{\partial \rho_w(T)}{\partial t} + \nabla[\rho_w(T)\mathbf{q}] = 0 \tag{1}$$

$$\mathbf{q} = -\frac{\mathbf{K}}{\rho_w(T)\mathrm{g}}[\nabla p - \rho_w(T)\,\mathrm{g}\,\nabla z] \tag{2}$$

$$[\varphi\rho_w(T)\ c_w + (1-\varphi)\rho_m c_m]\frac{\partial T}{\partial t} + \rho_w(T)c_w\mathbf{q}\nabla T = \nabla\{[\varphi\lambda_w + (1-\varphi)\lambda_m]\nabla T\} \tag{3}$$

where $\mathbf{q}$, p and T are the unknown Darcy flux, pressure and temperature, respectively. $\mathbf{K}$ denotes the two-dimensional hydraulic conductivity tensor,

$$\mathbf{K} = \begin{pmatrix} K_{xx} & 0 \\ 0 & K_{zz} \end{pmatrix} \tag{4}$$

while other parameters characterizing the numerical model are listed in Table 1. The temperature-dependent water density, which is given by a third-degree polynomial of the temperature (Weast, 1980; Molson and Frind, 2017), is

$$\rho_w(T) = \rho_r\{\ 1 + [-6.562\cdot10^{-6} + 2.166\cdot10^{-8}(T - T_r)](T - T_r)^2\} \tag{5}$$

where the reference water density is $\rho_r = 1000\,\mathrm{kg/m^3}$ at a reference temperature of $T_r = 4\,^{\circ}\mathrm{C}$. The effect of the temperature-dependent viscosity of pore water was not investigated within the framework of the recent study, but its effect on the phenomena is presented in the

Table 1
Model parameters. Bold marks the studied variables.

Definition	Symbol	Value	Units
Width of the model domain	L	6000	m
Depth of the model domain	$\boldsymbol{d}$	**500–5000**	**m**
Angle of the water table slope	γ	**0–5**	°
Reference temperature	T_r	4	°C
Surface temperature	T_s	10	°C
Bottom temperature	$\boldsymbol{T_b}$	**10–160**	**°C**
Porosity of the medium	φ	0.2	–
Horizontal hydraulic conductivity	K_{xx}	10^{-5}	m/s
Anisotropy coefficient	$\boldsymbol{\varepsilon}$	**0.1–100**	**–**
Reference water density	ρ_r	1000	kg/m^3
Thermal conductivity of water	λ_w	0.6	W/(m·K)
Specific heat of water	c_w	4200	J/(kg·K)
Matrix density	ρ_m	2600	kg/m^3
Thermal conductivity of matrix	λ_m	3.6	W/(m·K)
Specific heat of matrix	c_m	900	J/(kg·K)
Gravitational acceleration	g	9.81	m/s^2

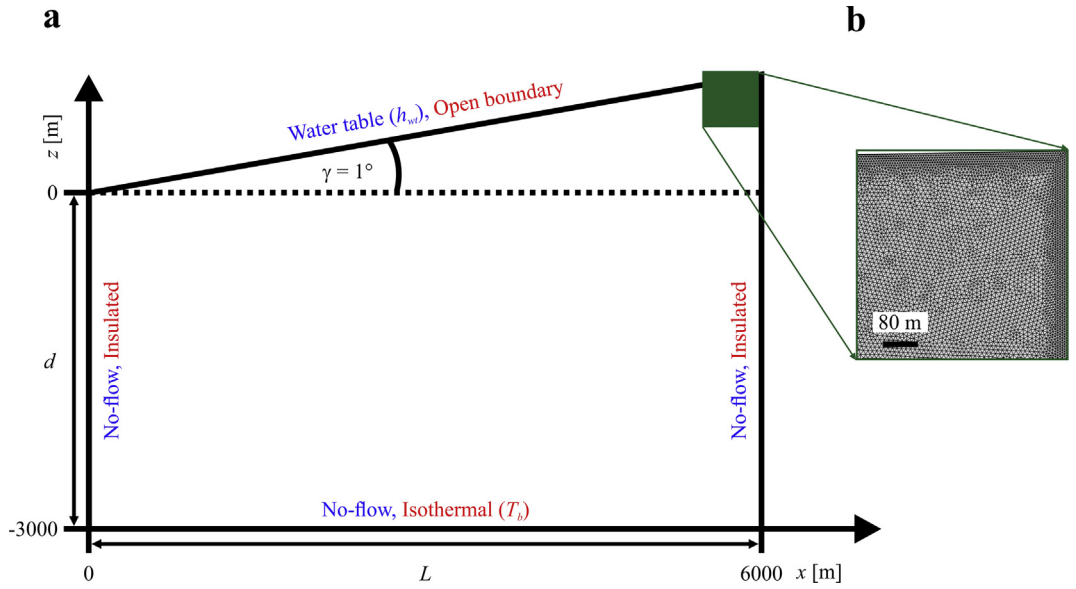

Fig. 1. (a) The model geometry with boundary conditions for flow (blue) and heat transfer (red). The vertical exaggeration of the slope is 10. (b) Illustration of the finite element discretization. (For interpretation of the references to colour in this figure legend, the reader is referred to the web version of this article.)

Table 2
Monitoring parameters.

Definition	Symbol	Units
Average Darcy flux	q_{av}	m/s
Average temperature	T_{av}	°C
Average vertical Darcy flux on the left-hand side	q_l	m/s
Average vertical Darcy flux on the right-hand side	q_r	m/s
Average horizontal Darcy flux at the bottom	q_b	m/s
Average hydraulic head	h_{av}	m

Supplementary material. Although using Darcy's Law is conventional in the case of a siliciclastic porous basin, it can also be used in fractured rocks and in karstified carbonate systems, where the use of equivalent porous media (EPM) approach is accepted (e.g. Lapcevic et al., 1999; Scanlon et al., 2003; Abusaada and Sauter, 2012; Mádl-Szőnyi and Tóth, 2015; Havril et al., 2016).

A simple two-dimensional basin model (similar to the original model of Tóth (1962)) was used as the isothermal base model. The upper boundary was a linear slope of the water table, as in the analytical solution found in Robinson and Love (2013) instead of a horizontal surface. Fig. 1a illustrates the applied homogeneous and isotropic base model with depth of $d = 3000$ m, width of $L = 6000$ m and constant regional water table slope of $\gamma = 1°$. A simple linear water table was applied during the simulations to highlight the pure interaction of two driving forces, i.e. the topography-driven forced and the buoyancy-driven free thermal convection. The flow boundary conditions were no-flow side and bottom boundaries, while the water table was prescribed on the surface,

$$h_{wt} = x \tan(\gamma) \tag{6}$$

where x denotes the horizontal coordinate and γ is the slope of the water table. Furthermore, the side walls were assumed to be thermally insulated, and an isothermal bottom boundary (T_b) was prescribed. The surface was considered as a thermally open boundary defined by the following relations,

$$T = \begin{cases} T_s & \text{if } \mathbf{n}\cdot\mathbf{q} < 0 \quad \text{(inflow)} \\ \mathbf{n}\cdot\mathbf{q_h} = 0 & \text{if } \mathbf{n}\cdot\mathbf{q} \geqslant 0 \quad \text{(outflow)} \end{cases} \tag{7}$$

where $T_s = 10$ °C is the initial surface temperature, $\mathbf{n}$ is the normal vector of the upper boundary pointing upward and $\mathbf{q_h}$ denotes the surface heat flux. The effect of different thermal boundary conditions for heat transfer (e.g. Lenkey, 1993; Domenico and Palciauskas, 1973; An et al., 2015; Han et al., 2015) were tested and presented in the Supplementary material. The initial condition for the time-dependent heat transfer problem was the conductive temperature distribution obtained from the stationary solution of Eq. (3) without the advection term ($\mathbf{q} = 0$).

In the course of the simulation, four model parameters were systematically altered with the aim of revealing the influence of thermal convection on the flow system The first investigated parameter was (1) the temperature difference between the bottom and the surface of the model ($\Delta T = T_b$-T_s, where ΔT varies from 0 to 50 °C) to study the role of thermal buoyancy. Further studied parameters were (2) the slope of the water table (γ = 0–5°), (3) the depth of the model (d = 500–5000 m) and (4) the anisotropy coefficient of the hydraulic conductivity ($\varepsilon = K_{xx}/K_{zz}$ = 0.1–100). The studied parameters are marked in bold in Table 1. Other model properties were kept constant during the simulation. The effect of these tested model parameters on groundwater flow was quantified by the monitoring parameters such as average values of the Darcy flux components, the hydraulic head and the temperature (Table 2). The monitoring parameters characterize changes in flow pattern and temperature field, additionally these parameters can be used to verify numerical models compared to measured head and temperature data.

The intensity of free thermal convection was characterized by the thermal non-dimensional Rayleigh number,

$$Ra = \frac{K_{av}\ c_w\ d}{\varphi\cdot\lambda_w + (1-\varphi)\cdot\lambda_m}[\rho_w(T_s) - \rho_w(T_b)], \tag{8}$$

where Ra is approximated by the water density difference between the upper and bottom boundary temperatures (Rabinowicz et al., 1998) and the average hydraulic conductivity is

$$K_{av} = \sqrt{K_{xx}K_{zz}} \tag{9}$$

which represents the geometric mean of diagonal elements of the hydraulic conductivity tensor (e.g. Zhang et al., 2007).

The system of partial differential equations given by Eqs. (1)–(3) was solved using the finite element numerical modeling software package, COMSOL Multiphysics 5.2 (Zimmermann, 2006) to compute the pressure, the temperature and the two components of the Darcy flux. The two-dimensional model domain was discretized by triangular

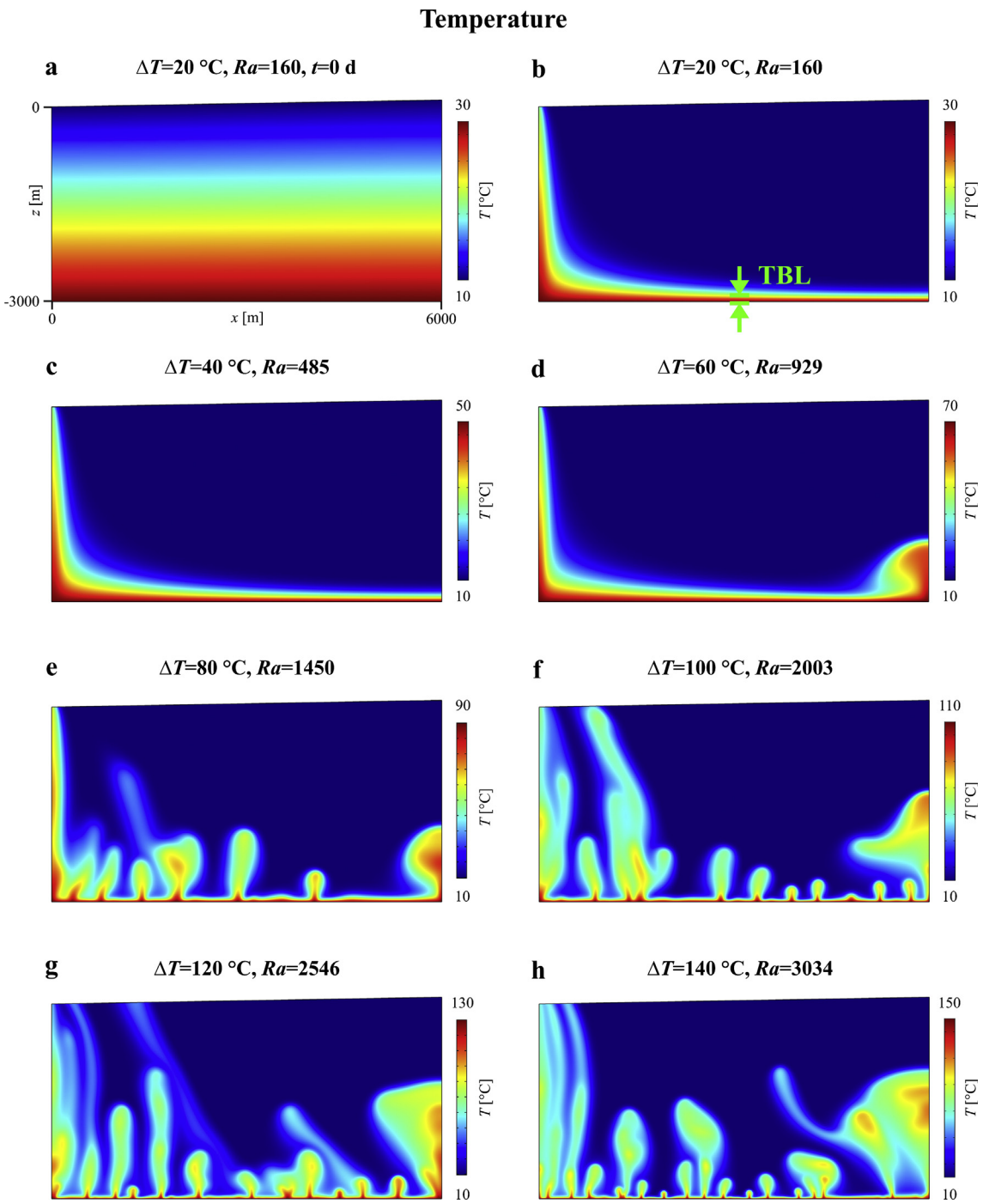

Fig. 2. (a) Initial conductive temperature field at ΔT = 20 °C and (b)–(h) temperature snapshots at a time of t = 11 kyr with a water table slope of γ = 1°, and temperature differences ranging from ΔT = 20 °C to 140 °C, representing the combined effect of forced and free thermal convection on the temperature field. The bottom thermal boundary layer (TBL) is illustrated in (b).

elements with non-uniform size (Fig. 1b) The maximum element size was 10 m in the model domain, which was reduced to 5 m along the boundaries to handle the high temperature gradient, for example in the thermal boundary layer (TBL). The final mesh had 588,521 finite elements in the base model (Fig. 1). The solution within the elements was approximated by quadratic Lagrangian polynomial functions. Generally, time-dependent simulations were performed at time-scales ranging from $t = 0$ to $5{\cdot}10^6$ days [d] (~13.7 kiloyears [kyr]) except for the investigation of the effect of anisotropy. This range proved sufficient to yield a stationary or quasi-stationary solution. In the first period ($t < 10^5$ d = 0.274 kyr), the time step increased exponentially, but thereafter remained constant at 1000 d. The time-dependent calculation for a given model run required approx. 1–7 days CPU time and 10–20 Gb memory on an Intel 2.79 GHz processor-based workstation.

3. Results and discussion

3.1. Effect of temperature difference

The temperature difference between the bottom and the surface of the model (ΔT) was systematically increased to investigate the combined effect of the driving forces of water table variation and heat

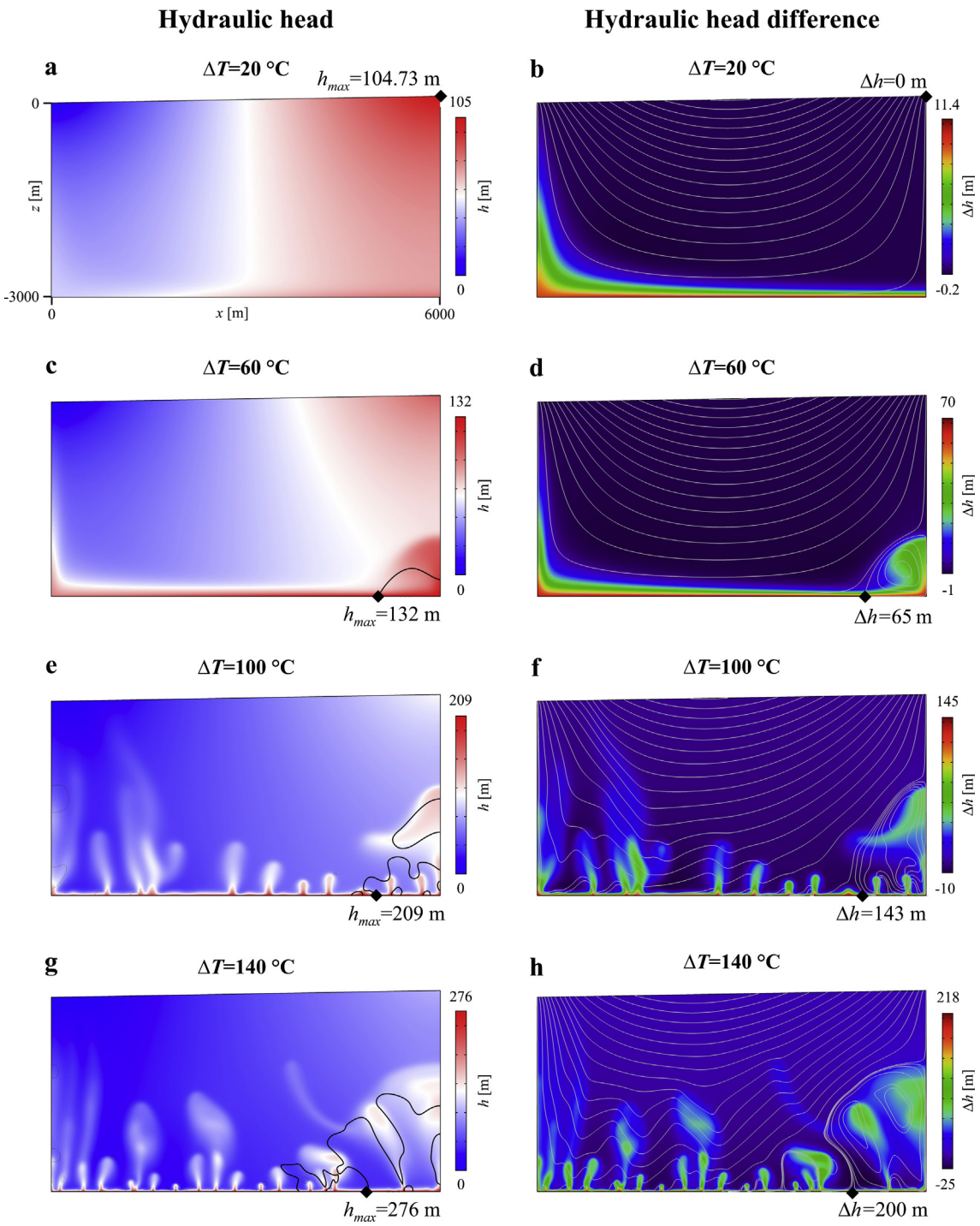

Fig. 3. Snapshots of the hydraulic head (h, left) and the hydraulic head difference ($\Delta h = h\text{-}h_0$, right) at $t = 11$ kyr, $\gamma = 1^\circ$ and at various temperature differences. Left (a, c, e, g): the black contour represents a zero horizontal Darcy flux, the head maximum is denoted by a black diamond. Right (b, d, f, h): the grey contours illustrate the Darcy flux streamlines, the head difference at the position of the maximum head is denoted by a black diamond.

transfer on the groundwater flow. First, this influence on the temperature distribution is displayed in Fig. 2, which shows the conductive initial temperature field at $t = 0$ d and $\Delta T = 20$ °C (Fig. 2a), and temperature snapshots at time $t = 11$ kyr, increasing ΔT from 20 °C to 140 °C (Fig. 2b–h). Fig. 3 (parallel to Fig. 2b, d, f and h) illustrates the distribution of the hydraulic head (h, left) and the hydraulic head difference between the calculated and the isothermal head at $\Delta T = 0$ °C ($\Delta h = h\text{-}h_0$, right) to show the influence of free thermal convection on head values. In the course of the investigation, the hydraulic head was determined according to the following formula,

$$h = \frac{p}{\rho_w(T)\,g} + z, \tag{10}$$

where z denotes the vertical coordinate.

Initially, the temperature of the pore water is determined by conduction over the entire numerical model, then is modified by topography-driven groundwater flow. With the applied model parameters (Table 1) the groundwater system converged towards a stationary solution when the temperature difference was $\Delta T < 60$ °C (Fig. 2b and c). In these cases the heat was advected toward the discharge area dominantly by topography-driven flow, so the effect of free thermal

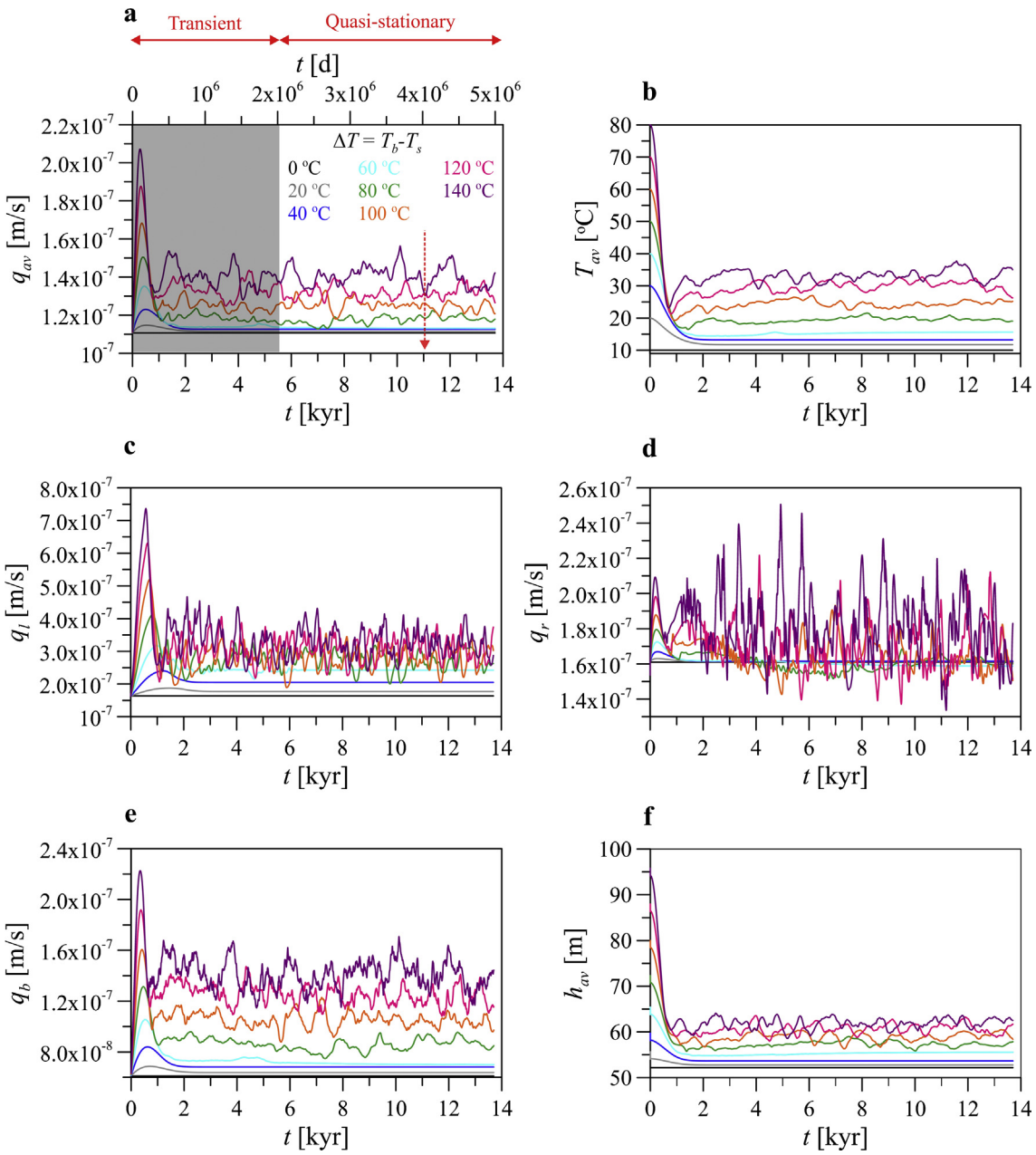

Fig. 4. Time series showing (a) the magnitude of the Darcy flux, (b) the average temperature, the vertical Darcy flux (c) on the left-hand and (d) on the right-hand side of the model domain, (e) the horizontal Darcy flux at the bottom and (f) the average hydraulic head of the model at various temperature differences. Temperature and hydraulic head snapshots in Fig. 2 and Fig. 3 are shown at $t = 11$ kyr which is marked with a red dashed arrow. Time-averaged values are calculated for the quasi-stationary time interval ($t > 5.48$ kyr). (For interpretation of the references to colour in this figure legend, the reader is referred to the web version of this article.)

convection seemed negligible compared to that of forced convection, which displays a certain similarity to the solution obtained by Domenico and Palciauskas (1973), and An et al. (2015). Consequently, the groundwater temperature beneath the recharge area was much lower than beneath the discharge area, closely approximating the surface temperature. The groundwater flow pattern was also characterized by a midline separating the recharge and discharge areas in the case of the isothermal base model, as established by Tóth (1962), and is illustrated by streamlines in Fig. 3b at $\Delta T = 20$ °C. Due to topography-driven flow the temperature distribution increases non-linearly with depth, and forced convection causes continuous hot upwelling beneath the discharge area, which is in agreement with the steady-state solutions of Smith and Chapman (1983) and An et al. (2015). The flow system shows a pattern similar to that of the isothermal base model; thus, the hydraulic head maximum ($h_{max} = 104.73$ m) is located at the highest point of the water table (Fig. 3a).

At a temperature difference of $\Delta T = 60$ °C, a stationary equilibrium evolved, as a thermal hot upwelling (plume) developed beneath the recharge area. Here thermal buoyancy is induced by the hot, low-density water upwelling from the bottom TBL (Elder, 1968; Turcotte and Schubert, 2002), which is balanced by the topography-driven, sinking cold water (Eq. (2)). A close relationship can be recognized between the positive temperature anomaly and the hydraulic head (see Fig. 2d and 3c, d). Modification of the groundwater flow system was especially evident within the long-lived right-hand side plume, where a local stationary convection cell developed. Consequently, the location of the maximum hydraulic head moved from the water table maximum to the TBL, and its value increased by about 27 m (Fig. 3c). However,

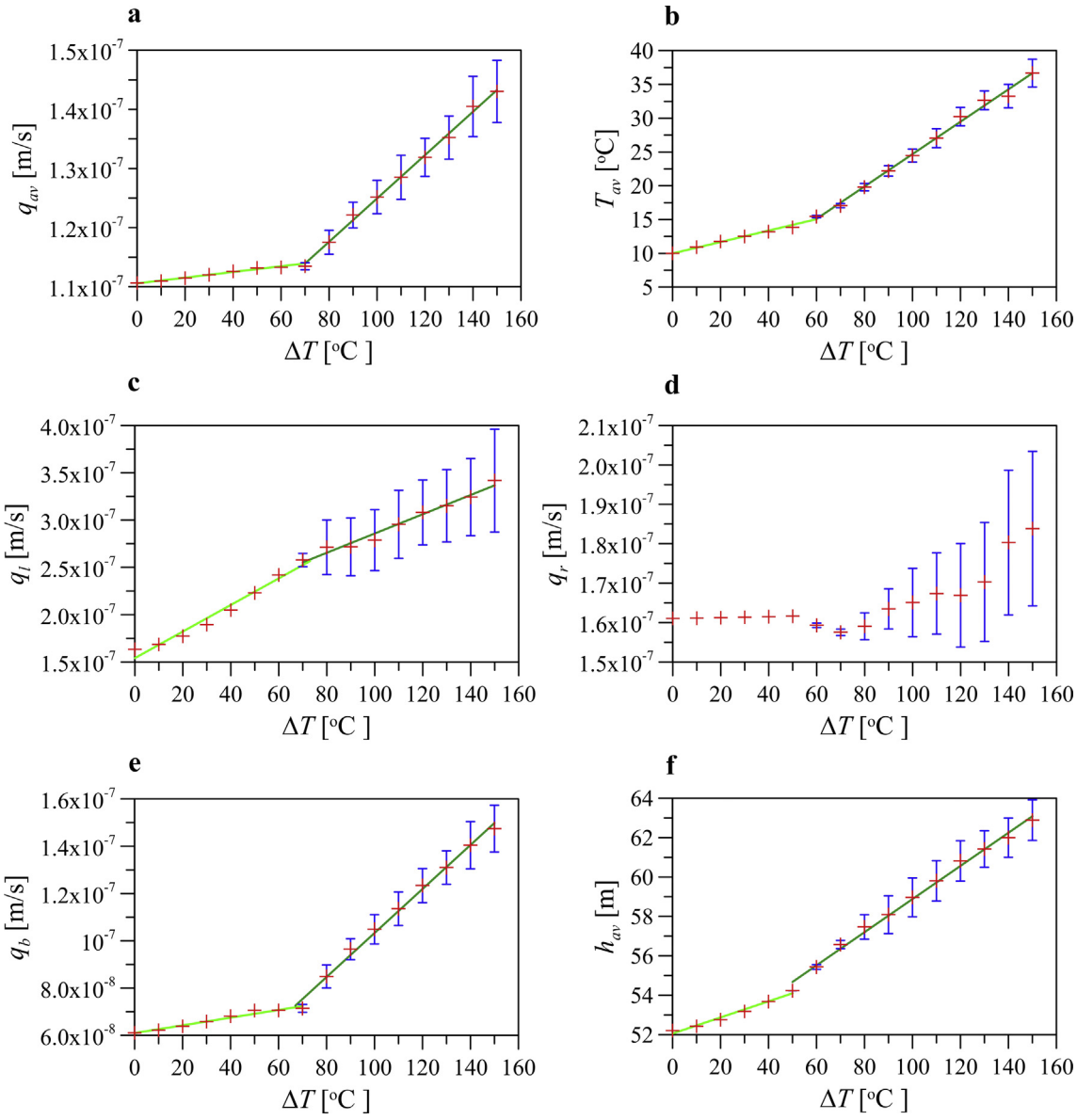

Fig. 5. Time-averaged values of the time series during the quasi-stationary time interval of (a) the Darcy flux, (b) the average temperature, (c) the vertical Darcy flux on the left-hand and (d) on the right-hand side, (e) the horizontal Darcyflux at the bottom and (f) the average hydraulic head plotted against the temperature difference. The standard deviations of the time series are denoted by blue bars. Fitted linear curves are denoted by green lines. (For interpretation of the references to colour in this figure legend, the reader is referred to the web version of this article.)

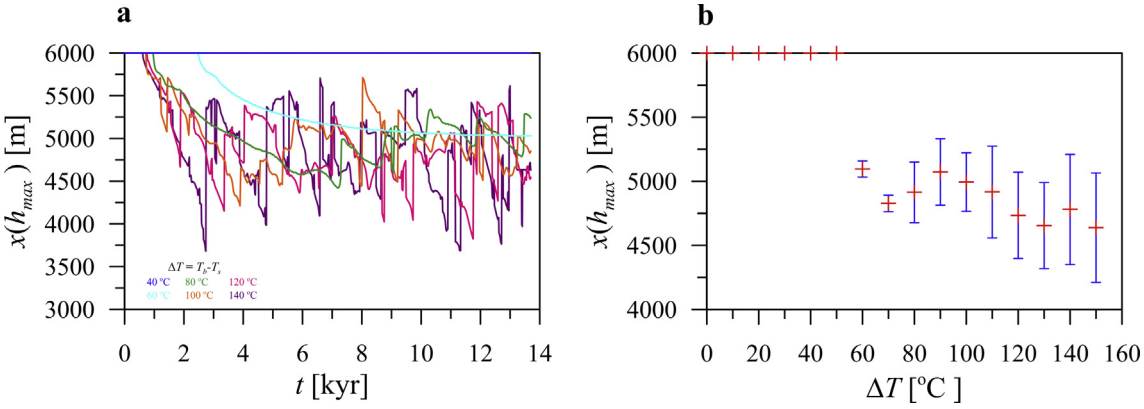

Fig. 6. (a) The horizontal position of the maximum hydraulic head as a function of time at different ΔT and (b) the average and the standard deviation of the horizontal position of the maximum hydraulic head plotted against temperature difference.

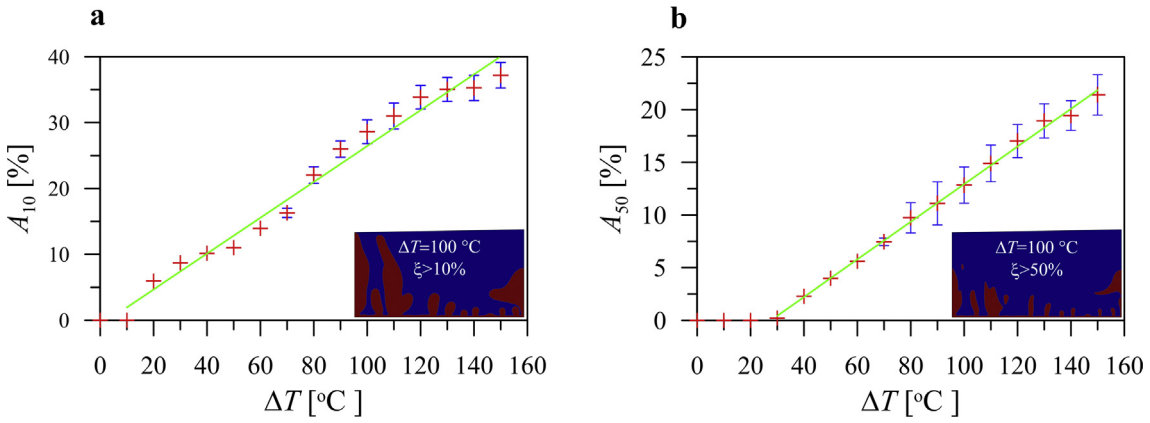

Fig. 7. The relative area of the model domain over which the hydraulic head is higher than that in the isothermal base model by at least (a) 10% (A_{10}), (b) 50% (A_{50}) as a function of the temperature difference. A linear curve was fitted to the values where the relative area exceeds 1%.

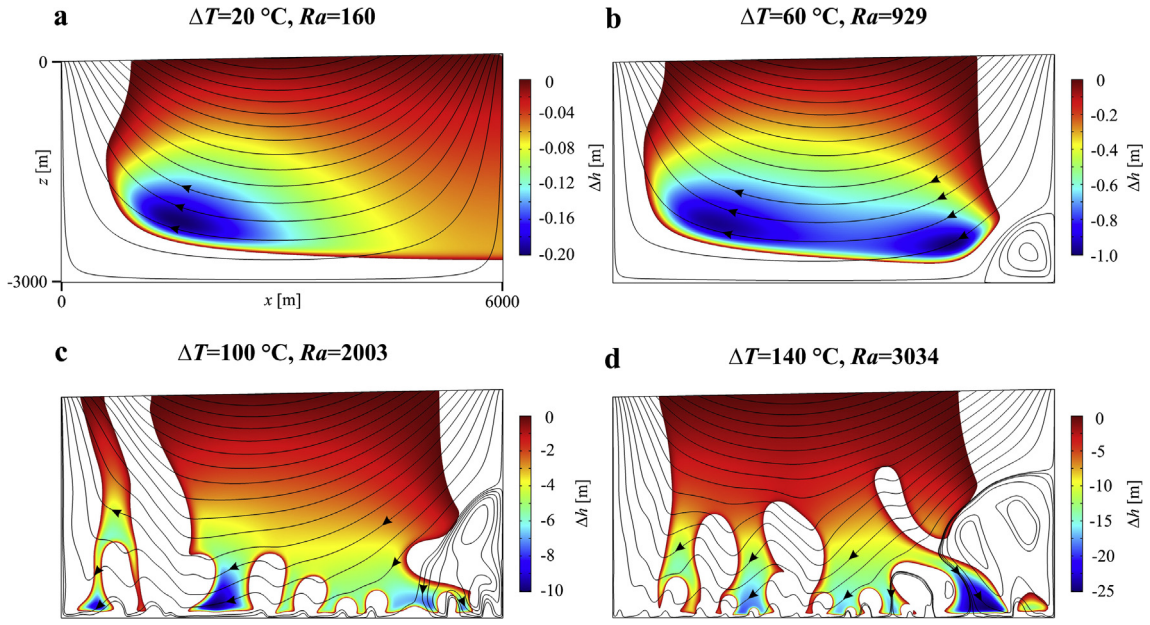

Fig. 8. Snapshots of hydraulic head decreases due to the effect of free thermal convection at various temperature differences ($\Delta h < 0$ at $t = 11$ kyr). The black contours illustrate the Darcy flux streamlines, the flow direction is represented by black arrows in the deeper part of the model.

the development of this steady-state local circulation did not cause any significant regional change in the flow pattern, except in the deeper zone of the recharge area. In this model, the approximate value of *Ra* was around 960 when the first effect of free thermal convection was seen.

A time-dependent flow system formed in scenarios in which ΔT was ≥ 70 °C ($Ra \geq 1183$). A pulsating long-lived hot plume evolved beneath the recharge area as a result of the formation of a dynamic equilibrium between the hot, buoyant upwelling and cold, dense downwelling water. The vertical movement of the plume became faster and more complex with increasing ΔT, which influenced the instability of the TBL. Therefore, free thermal convection promoted the formation of smaller hot upwellings; these, in turn, were swept towards the discharge area by the regional groundwater flow. Due to the open thermal boundary condition, the heat could transfer across the surface of the discharge area. Generally, due to the vigorous time-dependent thermal convection, the hydraulic head, h, and its difference from the solution in the isothermal base model, Δh, were significantly modified (Fig. 3e–h), especially in the deeper zone of the model basin and beneath the recharge area, where the previously-mentioned large convection cell evolved. Beneath the discharge area, forced and free thermal convection are superimposed, producing a permanent but time-variable upwelling. In addition, the maximum point of the hydraulic head migrated along the bottom of the model (in TBL) under the recharge zone, even reaching a value of $h_{max} = 276$ m (at $\Delta T = 140$ °C), approx. 171 m higher than in the isothermal base model (Fig. 3g). Free thermal convection was seen to qualitatively modify the effect of forced convection, not only through the temperature field but also through the heads and the flow pattern in some parts of the basin. However, further calculations were required to investigate the time-dependent behavior of the numerical model in detail.

In Fig. 4, the analysis of the time series is shown over a time interval of $t = 0$–13.7 kyr at various temperature differences, ΔT ranging between 0 and 140 °C. In the isothermal base model ($\Delta T = 0$ °C), the monitoring curves illustrate the steady-state flow system. Similarly, stationary solutions were obtained for all parameters when $\Delta T \leq 60$ °C after the transient time period ($t > 5.48$ kyr), while the initial conduction-generated temperature field (Fig. 2a) was considerably altered by forced thermal convection (e.g. Fig. 2b). As thermal buoyancy was enhanced with increased ΔT, the average temperature, hydraulic head and velocity components (except for q_r) converged to higher values.

Time-dependent solutions were found when the temperature

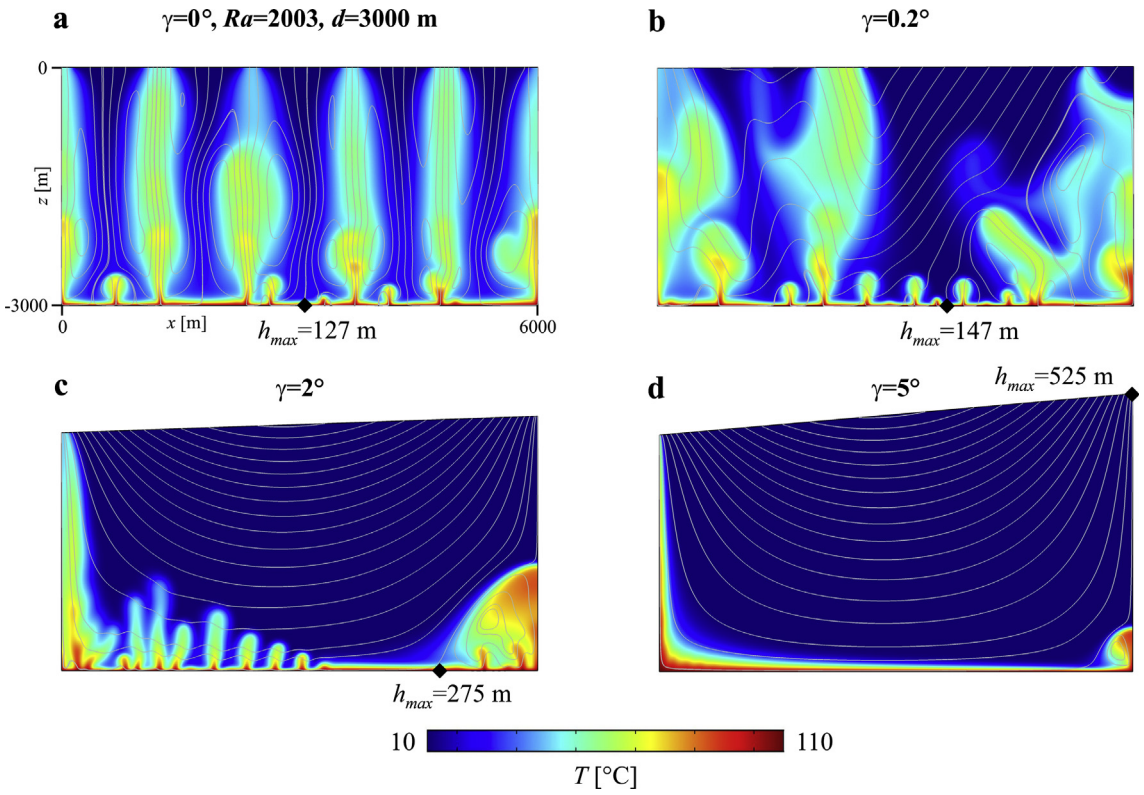

Fig. 9. Temperature snapshots at a time of t = 11 kyr and ΔT = 100 °C, the water table slope ranges from γ = 0° to 5°. The grey contours illustrate the Darcy flux streamlines, the maximum head is denoted by a black diamond.

difference was $\Delta T > 60$ °C. Beyond the transient behavior, the monitoring parameters tended towards a quasi-stationary solution. Higher ΔT intensified the flow, heated the model up and increased the hydraulic head. Fig. 4c and d and e represent the magnitude and the fluctuation of the Darcy fluxes due to the continuous upwelling beneath the discharge area, the pulsation of the long-lived plume beneath the recharge area, and the horizontal drift of the evolving plumes at the bottom TBL, respectively. The fluctuation of q_r is much more pronounced than that of the other time series, which represents the 'competition' between the cold downwelling and the rising hot plume. It should be noted that the quasi-stationary average temperature developed in the numerical models is much lower than the initial temperature (Fig. 4b) owing to the effective advective cooling furnished by forced convection. The slight increase in the average temperature also resulted in an increase in the hydraulic head (Fig. 4f), for instance, differences from the average hydraulic head in the isothermal base model (h_0 = 52 m) are about 3 m and 10 m at ΔT = 60 °C and 140 °C, respectively.

The gradient of the fitted curve changed at about ΔT = 60 °C in the average temperature and hydraulic head when the solution is still stationary, but a new hot plume emerged beneath the recharge zone (Fig. 2d). The change in the Darcy flux occurs rather at $\Delta T \cong 70$ °C, at which point free convection produces a time-dependent flow. Free convection induces further hot plumes rising from the bottom TBL, which can reach the surface before they merge into the left continuous upwelling, decreasing the buoyancy force and the vertical velocity along the left-hand side of the model. This mechanism causes the decrease in the rate of the curve fitted on q_l values (Fig. 5c).

Particular attention was given to the position of maximum hydraulic head (h_{max}), which was noticed at the water table maximum when $\Delta T \leq 50$ °C, that is, when forced thermal convection governs the steady-state system. In the scenarios in which the temperature and flow field were considerably modified ($\Delta T \geq 60$ °C), the position of the maximum head migrated to the bottom of the basin near the right-hand side upwelling (e.g. Fig. 3c and d). The position of h_{max} always coincides with the contours where the horizontal Darcy flux is zero (black contour, left) and the streamline touches the bottom boundary (grey contours, right). This proves that for a regime influenced by free thermal convection, h_{max} is situated at a local downwelling within the bottom TBL which separates the flow toward the recharge and the discharge zones, as a divergent stagnation point or a zone in the flow system. Fig. 6a illustrates the horizontal position of the maximum head (x(h_{max})) at several temperature differences as a function of time. Fig. 6b shows the time-averaged position of $x(h_{max})$ with its standard deviation. As free thermal convection intensifies, the position seems inclined to move toward the midline zone, which might be the final state with negligible forced convection (Fig. 3a, c, e, g).

After studying the time series of the monitoring parameters, the variation in the hydraulic head was used to facilitate the determination of the rate of the two different driving forces. Fig. 3 (right side) shows the hydraulic head difference compared to the purely topography-driven isothermal solution ($\Delta h = h\text{-}h_0$). Generally, Δh reaches 40–100 m, or even 100–218 m near the TBL, and inside the large plumes, where significant changes in groundwater flow are also noticed (e.g. right bottom corner). Fig. 7a and b show the relative area where the head has increased by at least 10% or 50%, respectively, owing to temperature. To be more exact, A_{10} and A_{50} denote the area related to the area of the model domain in which

$$\xi = 100\left(\frac{h}{h_0} - 1\right) \tag{11}$$

exceeds 10% or 50%, respectively. The thermal convection (forced and/or free) increases the head difference degrees, and either modifies ($\xi \geq 10\%$) or dominates ($\xi \geq 50\%$) the flow.

Clearly, in isothermal models there is no head difference, i.e. $A_{10} = A_{50} = 0\%$. The relative area of the model domain, where the hydraulic head is higher than that in the isothermal model by at least 10% (A_{10}), is shown in Fig. 7a. The figure indicates that at a

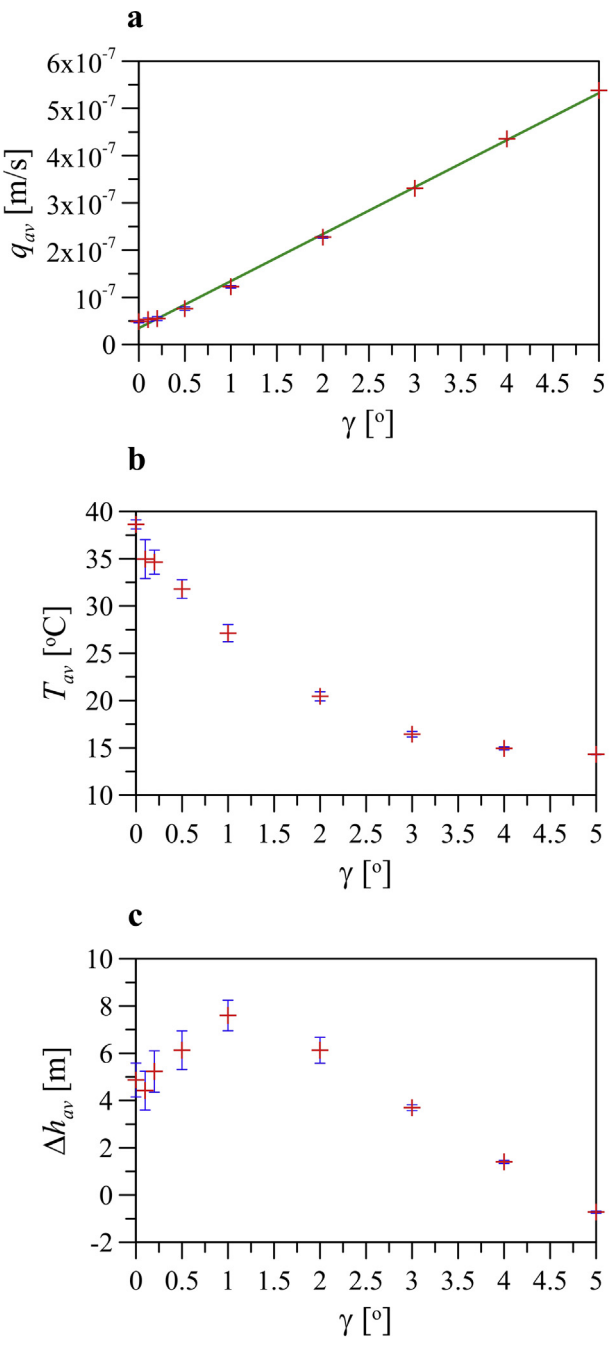

Fig. 10. Time-averaged values of the time series during the quasi-stationary time interval of (a) the Darcy flux, (b) the average temperature and (c) the difference between calculated and isothermal hydraulic head as a function of the water table slope (γ). The standard deviations of the time series are denoted by blue bars. The fitted linear curve is denoted by a green line (a). (For interpretation of the references to colour in this figure legend, the reader is referred to the web version of this article.)

temperature difference of $\Delta T = 20$ °C, the hydraulic head increases over approx. 6% of the area of the model domain due to thermal convection. This value reaches 37% for $\Delta T = 150$ °C. The transition from a forced convection dominated to a free convection dominated state is seen at $\Delta T = 60$–70 °C, but a linear function can be fitted onto the interval $\Delta T = 10$–150 °C. The relative area of the model dominated by thermal convection (A_{50}) (Fig. 7b) exceeds 2% at $\Delta T = 40$ °C and reaches 21.5% at $\Delta T = 150$ °C. The linear function was fitted over temperature differences ranging from 30 °C to 150 °C. The transition between the two types of convection can be detected only in the increased standard deviation. The inset in Fig. 7 emphasizes that significant hydraulic head differences exist around the pulsing plume beneath the recharge area, in the area surrounding the edge of the discharge zone, and in the deeper parts of the midline zone. In the upper part of the recharge and midline areas the water table variation drives the groundwater flow in the homogeneous, isotropic model.

Finally, it should be noted that thermal convection results not only in head increases due to the formation of a positive temperature anomaly (as was shown in Fig. 3, right), but also results in head decreases. Fig. 8 illustrates the head differences where these values are negative ($\Delta h \leq 0$), and snapshots were taken of several temperature differences. In stationary solutions (Fig. 8a and b) the negative anomalies (0– −1 m) are located near the plume roots (cf. Fig. 2b and d) due to the conservation of mass. Hot plumes strengthened by thermal buoyancy need some extra fluid, which is drawn away from the topography-driven flow system, producing local head minima. Thus, these minima represent local downwellings compared to the situation noticed in the isothermal simulation. This can also be seen in the time-variable systems (Fig. 8c and d). Hot plumes are fed by local downwellings, and the necessary extra mass is 'stolen' from the topography-driven groundwater flow system, resulting in head minima in the areas surrounding plume roots. In an evolving strongly time-dependent flow system (Fig. 8d), the head decrease (0 – −25 m) can be explained only by the dynamic effect of free thermal convection.

3.2. Effect of the water table slope

Both theoretical analyses and field observations suggest that the variation in water table slope is the most obvious parameter which is able to influence the hydrogeological processes in sedimentary basins (e.g. Freeze and Witherspoon, 1966, 1967; Tóth, 2009; Yang et al., 2010; Robinson and Love, 2013). Therefore, the slope angle of the linear water table (Eq. (6)) was systematically varied from γ = 0° to 5° while the temperature difference between the bottom and the surface was fixed at $\Delta T = 100$ °C to investigate the impact of increasing regional relief on the groundwater flow system. Fig. 9 depicts temperature snapshots at time $t = 11$ kyr and different values of γ.

Without any water table differences (Fig. 9a) the effect of forced convection does not exist, thus the flow pattern is controlled by pure free thermal convection. In the case of γ = 0°, five large plumes with a characteristic distance of 1200 m evolve after the transient period ($t > 5.48$ kyr). This value is considerably shorter than the wavelength of the instability at the onset of free thermal convection ($2.73d \approx 8190$ m) determined by Lapwood (1948). The discrepancy is explained by (1) the Rayleigh number for the model significantly exceeds the critical value ($Ra = 2003 > > Ra_{cr} \approx 27.1$) and (2) the upper boundary is thermally open. The flow and temperature field is time-dependent, thermal instabilities initiate from the bottom TBL, drift and merge into quasi-stationary hot upwellings. With increasing γ, forced thermal convection appears and can modify the temperature and Darcy velocity field, plumes are retained and a cold domain widens in the midline zone. For the model of γ = 5°, forced thermal convection dominates the system, producing two stationary upwellings along the model sides. This solution is analogous to the model of γ = 1° and $\Delta T = 60$ °C (Fig. 2d). The flow system is similar to the isothermal solution apart from the bottom corners of the model domain, and the maximum hydraulic head jumps back to the highest point of the water table ($h_{max} = 525$ m for γ = 5°).

Fig. 10 shows the time-averaged value and the standard deviation of the time series of the Darcy flux (q_{av}), the average temperature (T_{av}) and the average hydraulic head difference between the numerical and the isothermal model (Δh_{av}). For a horizontal water table (γ = 0°) the Darcy flux is approx. $5 \cdot 10^{-8}$ m/s and is generated purely by buoyancy forces (Fig. 10a). As γ increases, the role of forced convection increases, Darcy flux values tend to a linear curve, which is in agreement with $q_{av} \sim |\text{grad } p| \sim \gamma$ in Eq. (2), at least for small values of γ. A higher water

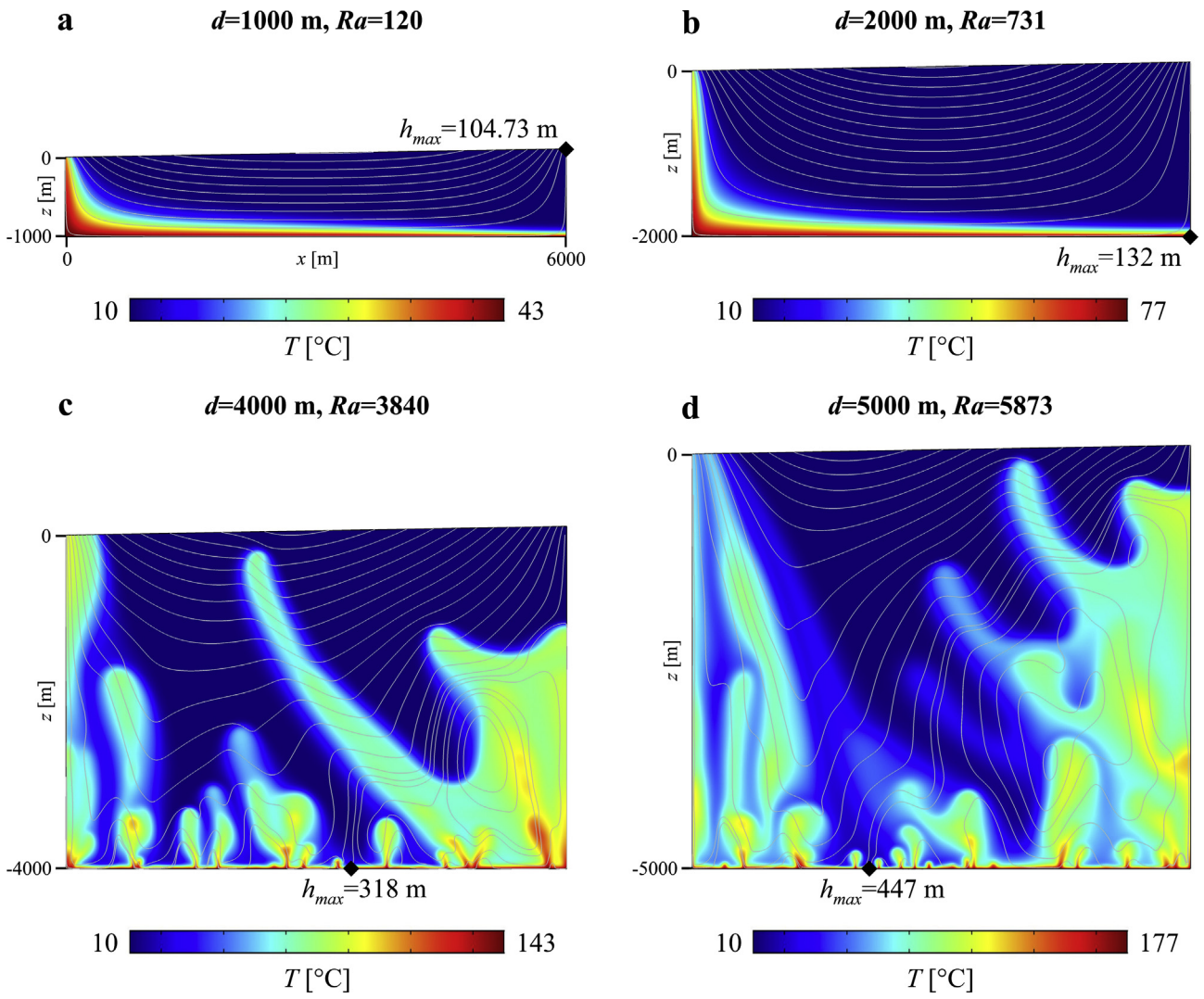

Fig. 11. Temperature snapshots at a time of t = 11 kyr, $\gamma = 1^{\circ}$ and increasing model depth with a uniform geothermal gradient (33.3 °C/km). The grey contours represent the Darcy flux streamlines, the head maximum is denoted by a black diamond.

table slope results in lower average temperature since enhanced forced thermal convection sweeps out the heat from the model (Fig. 10b). The average hydraulic head data are not shown because they vary with γ and so the dynamic effects are overshadowed. Thus Fig. 10c illustrates the average head difference from the isothermal models. For lower values of γ the hydraulic head difference increases, suggesting that free and forced thermal convection act coherently, and Δh_{av} reaches about 8 m at $\gamma = 1^{\circ}$. However, at values of $\gamma > 1^{\circ}$, Δh_{av} decreases owing to the reduced plume flux and tends to zero. The standard deviation of the computed monitoring parameters decreases with γ, as the groundwater flow system approaches steady-state condition.

3.3. Effect of model depth

Another crucial parameter, which significantly influences the flow system in a non-isothermal model, is the depth of the model domain. In our simulations the model depth was varied in the interval of d = 500–5000 m, while the temperature gradient between the bottom and the surface was constant, $\Delta T/d$ = 33.3 °C/km to keep comparability with the reference model (d = 3000 m, $\gamma = 1^{\circ}$ and ΔT = 100 °C, see Fig. 2f). The water table slope was fixed as well, at $\gamma = 1^{\circ}$.

Fig. 11 illustrates the effect of the growing model depth on the temperature field. For shallower model domains, with $d \leq 2000$ m, the solution is steady-state, where forced thermal convection due to topography-driven flow prevails over the system, resulting in one hot upwelling within the discharge zone. As the model deepens (and Ra increases owing to the growing water density difference and model depth), time-dependent free thermal convection appears, then starts dominating the groundwater flow, at least qualitatively.

The averaged time series of q_{av}, T_{av}, and h_{av} quantify the impact of the model depth on the monitoring parameters (Fig. 12). First, the Darcy flux decreases with d since the flow is less intense in a deeper model domain (Fig. 12a and b). However, when free thermal convection appears (d = 2500 m, Ra = 1284), the rate of the decrease slows, then reverts to a slight increase, because thermal buoyancy predominates over a greater proportion of the model domain, especially in the deep zones (Fig. 11c and d).

The average model temperature increases slightly in the stationary, forced thermal convection regime ($d \leq 2000$ m) (Fig. 12b). When free thermal convection begins, the gradient of the fitted linear curve becomes steeper, reflecting warming in the deep mid-line zone and beneath the recharge area. The trend of average hydraulic head is similar to the temperature variation (Fig. 12c), which confirms that the reduction in water density due to the temperature increase is responsible for the head growth. Nevertheless, the standard deviation of the time series reflects the variability of the system due to time-dependent free thermal convection.

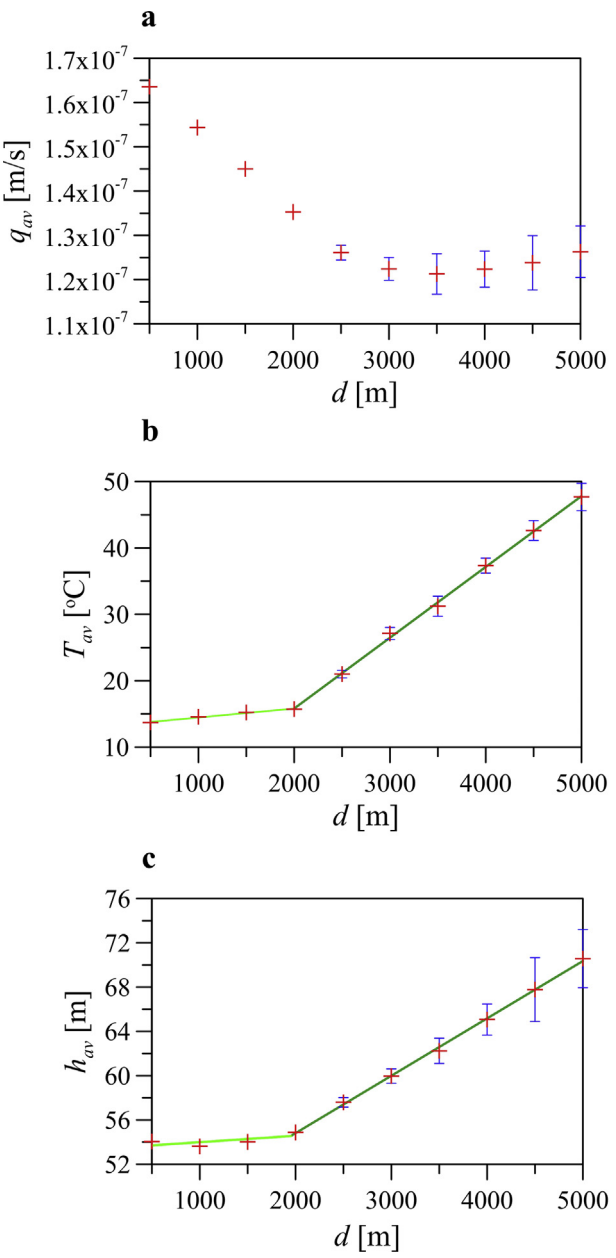

Fig. 12. Time-averaged values of the time series during the quasi-stationary time interval of (a) the Darcy flux, (b) the average temperature and (c) the average hydraulic head plotted against the model depth. The standard deviations of the time series are denoted by blue bars. The fitted linear functions are denoted by green lines. (For interpretation of the references to colour in this figure legend, the reader is referred to the web version of this article.)

3.4. Effect of anisotropy of hydraulic conductivity

The anisotropy of the hydraulic conductivity ($\varepsilon = K_{xx}/K_{zz}$) can reach 100–1000 in siliciclastic sedimentary basins, depending on the stratification of clayey and sandy layers, grain orientation etc. However, the anisotropy in fractured carbonates is usually quite different because (1) large anisotropy rates are less probable due to the more homogeneous matrix composition, and (2) a ratio of $\varepsilon < 1$ can occur as well owing to vertical fracturing. Thus, the effect of the anisotropy ratio was studied in the range of $\varepsilon = 0.1$–100. Since an increase of anisotropy slows down the flow considerably, the length of simulations was increased depending on ε to obtain a quasi-stationary solution. Other parameters correspond to the reference model (Fig. 2f).

It is clear based on Fig. 13 that an anisotropy of $\varepsilon < 1$ facilitates vertical groundwater flow, which favors buoyancy-driven free thermal convection over forced convection. As ε increases (i.e. vertical hydraulic conductivity decreases), free thermal convection is repressed by topography-driven flow. The high Darcy flux zone narrows toward the surface, where the flow is dominantly horizontal. In the deeper domain, sluggish, periodic ($\varepsilon = 20$, Fig. 13e) or almost stationary convection ($\varepsilon = 100$, Fig. 13f) forms. The two flow systems separate in the homogeneous model, where the upper part of the model is controlled by topography-driven flow, while the lower part is governed by buoyancy-driven flow. With increasing ε, the head maxima decrease as a dynamic consequence of the slowing flow.

The averaged Darcy flux time series support the qualitative observation that the high anisotropy retains the flow (Fig. 14). On the average Darcy flux data, a $1/\sqrt{\varepsilon}$ function was fitted, since $q_{av} \sim K_{av} \sim K_{xx}/\sqrt{\varepsilon}$ (see Eqs. (2) and (9)). The average temperature and — in parallel— the average hydraulic head, both increase with ε. The model domain becomes warmer owing to the sluggish flow in the deeper zone. Separation of the topography- and buoyancy-driven flow system at about $\varepsilon \geq 5$ is distinctly visible in Fig. 14b and c. The values of T_{av} and h_{av} depend strongly on the type of flow regime which evolves in the deep zone, either quasi-periodic characterized with lower temperatures and heads ($\varepsilon = 5$, 20), a slow-moving, sluggish with system higher temperatures and heads ($\varepsilon = 10$, 50), or an almost stationary system with low standard deviation ($\varepsilon = 100$). Last, we note that, on the one hand the maximum head decreases with ε due to the slowing flow (dynamic effect, Fig. 13), on the other hand the average head increases with ε (thermal effect, Fig. 14c).

3.5. Modified Péclet number

Where the equivalent porous media approach is valid, the quantitative evaluation of the combined effect of forced and free thermal convection requires the use (e.g. Patankar, 1980; Clauser and Villinger, 1990) and/or the definition of a non-dimensional number. Therefore besides the thermal Rayleigh number, the non-dimensional modified Péclet number was defined which facilitates the classification of the flow systems into forced and free thermal convection-dominated state, with respect to advective/convective and conductive transport processes:

$$Pe^* = \frac{\rho_w(T)c_w \ \Delta q d}{\varphi \cdot \lambda_w + (1-\varphi)\cdot\lambda_m} \tag{12}$$

where Δq is the magnitude of Darcy flux reduced by the purely topography-driven isothermal ($\Delta T = 0$ °C) Darcy flux ($\Delta q = q_{av} - q_0$).

Fig. 15 illustrates the Rayleigh number (Ra) as a function of the modified Péclet number (Pe^*) for the evaluation of all the simulated scenarios. Transition from steady-state forced thermal convection to time-dependent free thermal convection appeared when the Rayleigh and the modified Péclet number were $Ra = 500$–1100 and $Pe^* = 10$–20, respectively. Below these intervals, the flow systems converge towards a steady-state solution, and forced convection is the dominant driving force (Fig. 2b–d; Fig. 9d; Fig. 11a, b; Fig. 13e and f), but above that, time-dependent free thermal convection intensifies the flow in the model basin (Fig. 2e–d; Fig. 9a–c; Fig. 11c, d; Fig. 13a–d).

Former interval means that the Rayleigh number is more than one order of magnitude higher than the critical value determined by Lapwood (1948). Latter represents that free thermal convection is expected when the Darcy flux obtained from non-isothermal model exceeds the Darcy flux obtained from isothermal model by at least one order of magnitude.

3.6. Effect of no-flow side boundaries

Finally, the influence of the side walls as no-flow boundaries was investigated. Impermeable side walls stabilize the flow, and facilitate

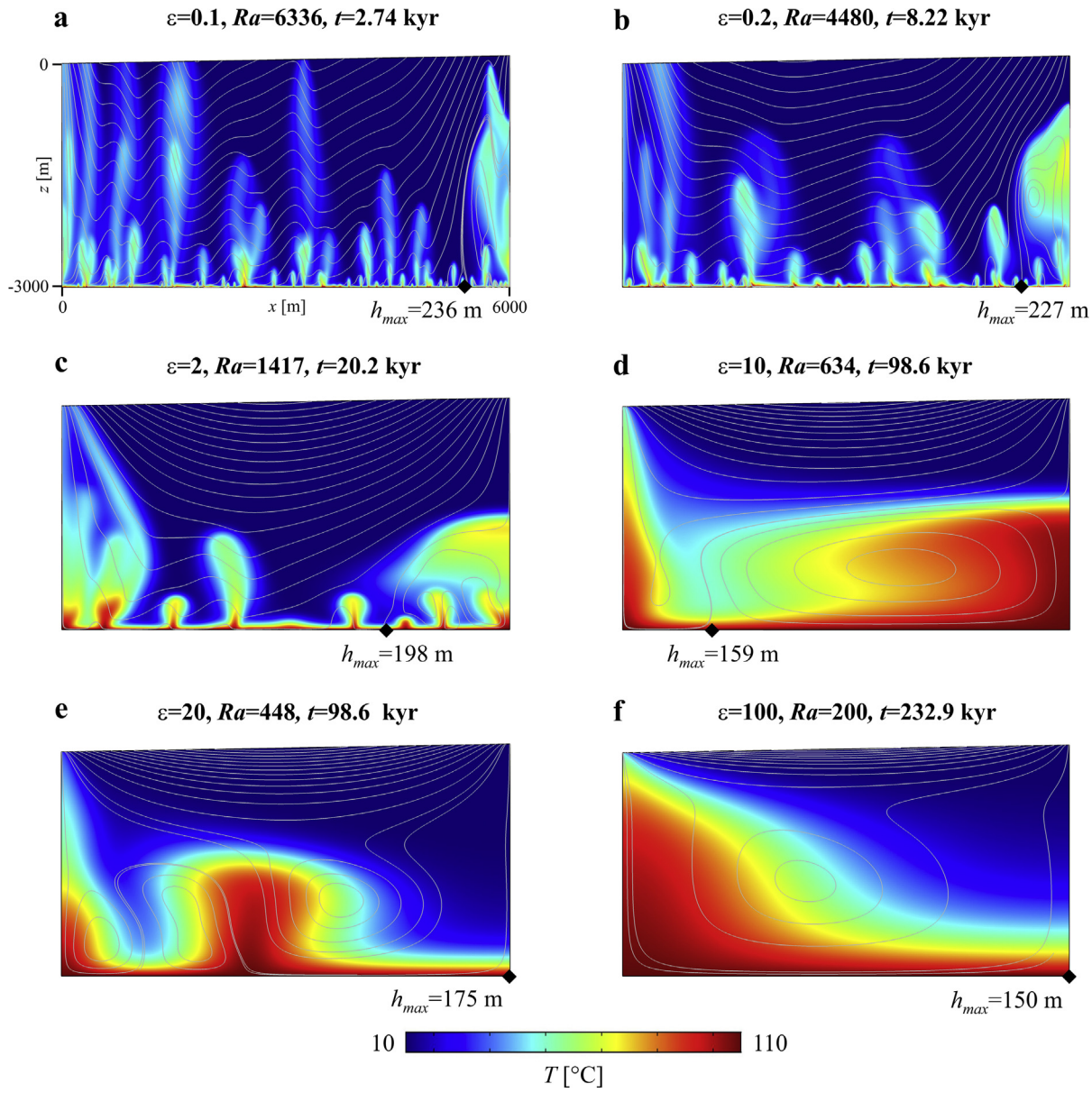

Fig. 13. Temperature snapshots at $\Delta T = 100$ °C, $\gamma = 1°$ and various hydraulic conductivity anisotropy values. The grey contours represent the Darcy flux streamlines, the maximum head is denoted by a black diamond.

formation of stable upwellings along the boundaries beneath discharge areas, and often beneath recharge areas. In order to eliminate this effect three domains were compiled into one model including a divide and a valley (Fig. 16). Other model parameters were the same as in the homogeneous, isotropic reference model, $\gamma = 1°$, $d = 3000$ m, $\Delta T = 100$ °C and $\varepsilon = 1$ (Fig. 2f).

Beneath the inner divide ($x = 12000$ m) neither a permanent nor an oscillating hot plume forms, but initial upwellings move left or right toward the inner or the outer valley, respectively. Plumes evolve and lengthen while they drift toward the discharge zones. Beneath the inner valley ($x = 6000$ m), plumes from the divides group and merge to arise in the main upwelling zone, however their positions are not fixed. Plumes forming along no-flow boundaries ($x = 0$ and 18000 m) show similar shapes as in the individual domain models. Clearly, no-flow side boundaries affect the time-dependent pattern of the flow and temperature field, however their impact on the behavior of the system and the averaged monitoring parameters is not significant. Fig. 14 shows the deviation in the averaged Darcy flux, temperature and hydraulic head values between the complex (black circle) and the reference (red cross, $\varepsilon = 1$) model.

4. Summary and conclusions

Finite element numerical model calculations were performed to investigate how buoyancy-driven free thermal convection influences topography-driven forced thermal convection in a synthetic groundwater basin. In order to focus on the combined process, a simple two-dimensional, homogeneous model domain was chosen with a linear water table slope in which the single variable material property was the water density depending on the temperature. The model simulation could also be applied as theoretical-physical experiments to understand processes occurring in siliciclastic sedimentary basins, fractured rocks or karstified carbonate systems.

First, the temperature difference between the bottom and the surface (ΔT) was varied. Due to increasing geothermal gradient the flow became more intense, and the change from forced thermal convection to a free thermal convection regime induced a significant increase in the gradient of the monitoring parameters (Fig. 5). The relative area

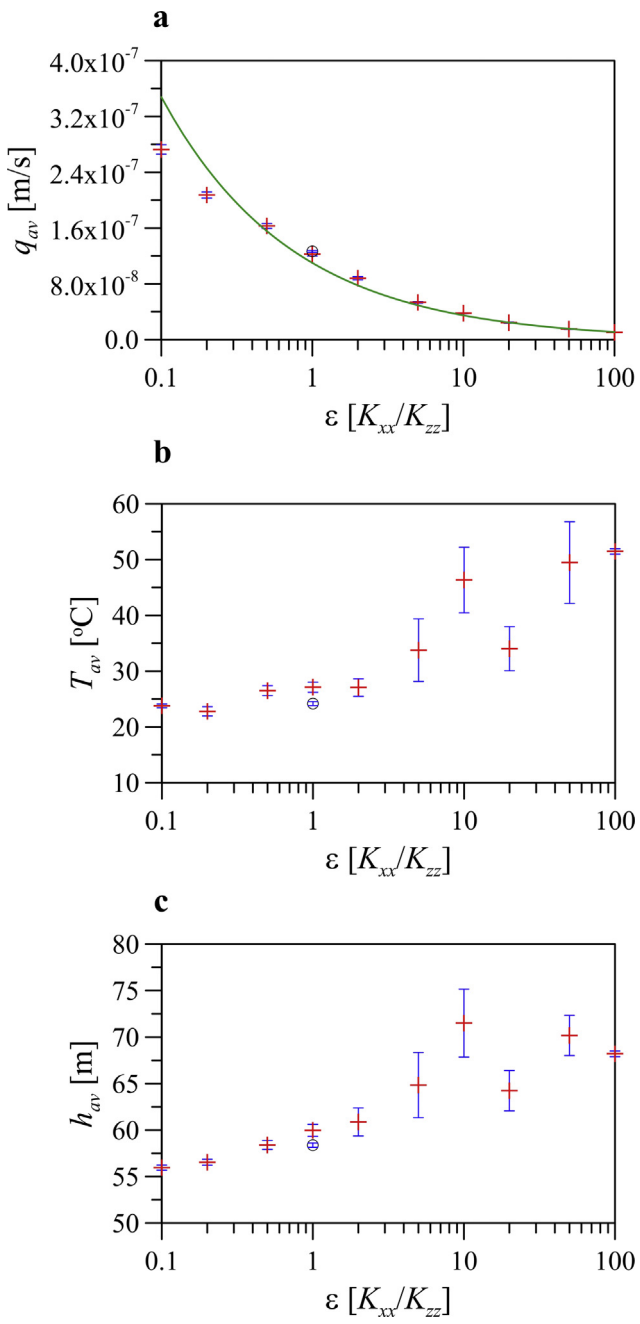

Fig. 14. Time-averaged values of the time series during the quasi-stationary time interval of (a) the Darcy flux, (b) the average temperature and (c) the average hydraulic head as a function of the increasing anisotropy coefficient. The standard deviations of the time series are denoted by blue bars. Fitted $1/\sqrt{\varepsilon}$ function is denoted by green lines (a). Black circles illustrate the solution of the complex model at $\varepsilon = 1$ (see Fig. 14). (For interpretation of the references to colour in this figure legend, the reader is referred to the web version of this article.)

modified/dominated by free thermal convection was enhanced ΔT (Fig. 7). Compared to the isothermal base model ($\Delta T = 0$ °C), the hydraulic head increased with ΔT due to the decreasing water density. Conversely, negative head differences also appeared, which can be explained only by the dynamic effect of the enhanced plume activity (Fig. 8). As a result of the increased temperature difference, intensive time-dependent free thermal convection evolved in the model basin.

The effect of the change of the slope of the water table within the range of $\gamma = 0$–5° at a constant temperature difference, $\Delta T = 100$ °C was also investigated. As γ increased, purely free thermal convection-

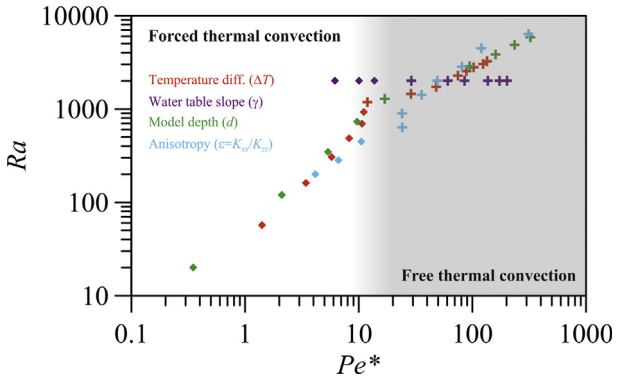

Fig. 15. Rayleigh number (Ra) versus modified Péclet number (Pe^*) for simulations with varying temperature difference (ΔT), water table slope (γ), model depth (d) and anisotropy of hydraulic conductivity ($\varepsilon = K_{xx}/K_{zz}$). The steady-state solutions are denoted by diamonds, the time-dependent solutions are denoted by crosses. Grey shading indicated the dominancy of free thermal convection.

governed flow transformed into forced thermal convection-dominated flow. As a consequence, the topography-driven groundwater flow intensified the Darcy flux resulting in effective advective cooling (Fig. 10). In other words, an increase in the water table slope facilitates forced thermal convection. Nevertheless, a simple linear water table was applied in the model, but this simplification helps to highlight the transition between free and forced thermal convection, and likely does not affect the transitional behavior.

The influence of depth of the model domain (d) was next investigated, while maintaining a uniform geothermal gradient (100 °C/km). For shallower model depths ($d \leq 2500$ m) stationary topography-driven thermal convection characterized the system, however, for deeper models the groundwater flow system became time-dependent due to the appearance of free thermal convection. Deeper models at constant geothermal gradient favor free thermal convection.

The anisotropy of the hydraulic conductivity ($\varepsilon = K_{xx}/K_{zz}$) was varied within $\varepsilon = 0.1$–100 including both values of $\varepsilon < 1$ representing e.g. carbonates with vertical fractures, and values of $\varepsilon > 1$ characterizing e.g. siliciclastic basins with mild and moderate anisotropy. On the one hand, increasing ε hinders vertical flow and suppresses free thermal convection due to reduced vertical hydraulic conductivity. On the other hand, higher anisotropy enforces topography-driven groundwater flow into the shallower region, which helps the separation of the two flow regimes (Fig. 13).

In this study, the flow system was investigated within a wide range of ΔT, γ, d, and ε values corresponding to the thermal Rayleigh numbers ($Ra = 0$–6336), and the modified Péclet numbers ($Pe^* = 0$–323). The effect of time-dependent free thermal convection only appeared in our simulations when $Ra \geq 500$–1100 and $Pe^* \geq 10$–20 (Fig. 15). Nevertheless, in sedimentary basins, combined topography- and buoyancy-driven groundwater flow system evolves at even infinitesimally low temperature differences, if the water table slope is $\gamma > 0$.

The removing of artificial no-flow boundaries at the side walls helped to elucidate their effect on the flow and temperature pattern by horizontally connecting the individual model domains. Although the flow and the temperature patterns changed in the complex model, the dynamics of the flow system and the quantitative character remained uniform (Fig. 16).

In the homogeneous model the position of the maximum hydraulic head (h_{max}) is always located at the highest point of the water level or within the bottom TBL. In the latter case the position of h_{max} corresponds to a divergent stagnation point (Tóth, 1988, 1999; Jiang et al., 2011; Wang et al., 2011) which moves and/or skips in the time-dependent system. A local downwelling overlies this point which is characterized by a local head minimum as a zone through which hot

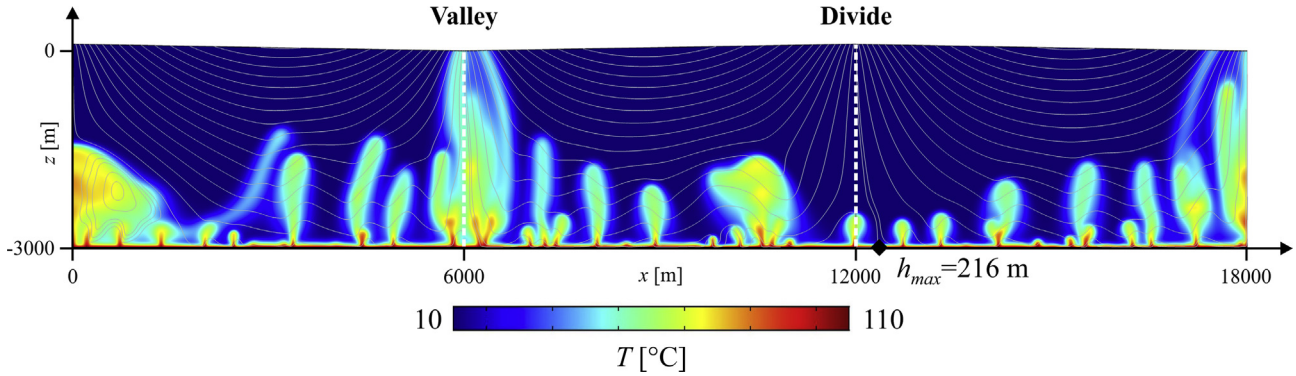

Fig. 16. Temperature distribution of the complex homogeneous, isotropic model containing three reference models (d = 3000 m, L = 6000 m, ΔT = 100 °C, γ = 1°, ε = 1) at a time of t = 11 kyr. The grey contours represent the Darcy flux streamlines, the maximum head is denoted by a black diamond. The inner divide and the valley areas are marked by dashed white lines.

plumes are fed by water.

Finally, we need to mention that the effects of numerous parameters and phenomena could not be investigated in this paper, which could modify the conclusions (e.g. model geometry, dispersion, heterogeneity, temperature-dependent viscosity, boundary conditions etc.). Some of these effects are discussed in the Supplementary material. We found that the effect of temperature-dependent viscosity intensifies the flow and facilitates free thermal convection. On the other hand, constant heat flux prescribed at the bottom boundary reduces flow system complexity, and favors forced thermal convection. Moreover we noted that the recharge rate in the simple base model is overestimated (≈5 m/yr), however the decrease of water table slope and the increase of anisotropy coefficient significantly reduces this recharge to an acceptable real range (e.g. 0.1–0.3 m/yr for γ = 0.1° and ε = 10, see Table S2 in the Supplementary material).

If we adapt the model results for real geological situations, the appearance of time-dependent thermal convection cannot be excluded in inverted basins beside the effect of gravity-driven groundwater flow. In areas where the geothermal gradient exceeds the mean value (e.g. due to the thin lithosphere approx. 50 °C/km in the Pannonian Basin (Lenkey et al., 2002, 2017) unsteady free thermal convection is likely to occur in deep karstified carbonates (Havril et al., 2016) or in faulted siliciclastic basins (Lopez et al., 2016).

The effect of free thermal convection can be observed in the vertical temperature distribution of deep carbonate regions (e.g. in the Buda Thermal Karst), where the temperature anomalies cannot be explained by either conduction or pure forced thermal convection (Mádl-Szőnyi et al., 2018). The results of the numerical simulations, for the combined effect of forced and free thermal convection, can be validated using basin-scale data evaluation methods, such as temperature elevation (T(z)), pressure elevation (p(z)) and total dissolved solids elevation (TDS(z)) profile, (e.g. Tóth, 2009; Mádl-Szőnyi and Tóth, 2015; Mádl-Szőnyi et al., 2017).

Combined topography- and buoyancy-driven groundwater flow in sedimentary basins can thus be characterized by very complex and time-dependent head and temperature patterns which complicate the processes, e.g. planning of an optimal geothermal well system. Geothermal studies in sedimentary basins cannot therefore focus only on the presence of a free or forced thermal convection as a single driving force.

Acknowledgements

The authors are grateful to László Lenkey for his useful remarks and thought-provoking comments. The detailed review of the manuscript by John Molson is widely appreciated and helped to improve the quality of the paper. The authors would like to thank the other anonymous reviewer for the helpful and appropriate advices. This research is part of a project that has received funding from the European Union's Horizon 2020 research and innovation program under grant agreement No 810980. The project was supported by the ÚNKP-18-3 New National Excellence Program of the Ministry of Human Capacities, and the Hungarian Scientific Research Fund (K 129279) and by the János Bolyai Research Scholarship of the Hungarian Academy of Sciences. This research was supported by the European Union and the State of Hungary, co-financed by the European Social Fund in the framework of TÁMOP 4.2.4. A/1-11-1-2012-0001 National Excellence Program.

Appendix A. Supplementary data

Supplementary data to this article can be found online at https://doi.org/10.1016/j.jhydrol.2019.03.003.

References

Abusaada, M., Sauter, M., 2012. Studying the flow dynamics of a karst aquifer system with an equivalent porous medium model. Ground Water 51 (4), 641–650. https://doi.org/10.1111/j.1745-6584.2012.01003.x.

An, R., Jiang, X.-W., Wang, J.-Z., Wan, L., Wang, X.-S., Li, H., 2015. A theoretical analysis of basin-scale groundwater temperature distribution. Hydrogeol. J. 23 (2), 397–404. https://doi.org/10.1007/s10040-014-1197-y.

Bear, J. Verruijt, A., 1987. Modeling Groundwater Flow and Pollution, 1st ed., Springer, Reidel, Dordrecht, Holland, pp. 414, http://dx.doi.org/10.1007/978–94–009–3379–-8, ISBN: 978–1–55608-015–9.

Bethke, C.M., 1985. A numerical model of compaction-driven gorundwater flow and heat transfer and its application to the paleohydrology of intracratonic sedimentary basin. J. Geophys. Res. 90 (B8), 6817–6828. https://doi.org/10.1029/JB090iB08p06817.

Bredehoeft, J.D., Papadopulos, I.S., 1965. Rates of vertical groundwater movement estimated from the Earth's thermal profile. Water Resour. Res. 1 (2), 325–328. https://doi.org/10.1029/WR001i002p00325.

Cardenas, M.B., Jiang, X.-W., 2010. Groundwater flow, transport, and residence times through topography-driven basins with exponentially decreasing permeability and porosity. Water Resour. Res. 46 (11), W11538. https://doi.org/10.1029/2010WR009370.

Cathles, L.M., Smith, A.T., 1983. Thermal constraints on the formation of Mississippi Valley-type lead-zinc deposits and their implications for episodic basin dewatering and deposit genesis. Econ. Geol. 78 (59), 983–1002. https://doi.org/10.2113/gsecongeo.78.5.983.

Clauser, C., Villinger, H., 1990. Analysis of conductive and convective heat transfer in a sedimentary basin, demonstrated for the Rheingraben. Geophysis. J. Int. 100 (3), 393–414. https://doi.org/10.1111/j.1365-246X.1990.tb00693.x.

Cserepes, L., Lenkey, L., 2004. Forms of hydrothermal and hydraulic flow in a homogeneous unconfined aquifer. Geophys. J. Int. 158 (2), 785–797. https://doi.org/10.1111/j.1365-246X.2004.02182.x.

Domenico, P.A., Palciauskas, V.V., 1973. Theoretical analysis of forced convective heat transfer in regional ground-water flow. GSA Bull. 84 (12), 3803–3814. https://doi.org/10.1130/0016-7606(1973) 84<3803:TAOFCH>2.0.CO;2.

Elder, J., 1967. Steady free convection in a porous medium heated from below. J. Fluid Mech. 27 (1), 29–48. https://doi.org/10.1017/S0022112067000023.

Elder, J., 1968. The unstable thermal interface. J. Fluid Mech. 32 (1), 69–96. https://doi.org/10.1017/S0022112068000595.

Freeze, R.A., Witherspoon, P.A., 1966. Theoretical analysis of regional groundwater flow: 1. Analytical and numerical solutions to the mathematical model. Water Resour. Res. 2 (4), 641–656. https://doi.org/10.1029/WR002i004p00641.

Freeze, R.A., Witherspoon, P.A., 1967. Theoretical analysis of regional groundwater flow: 2. Effect of water-table configuration and subsurface permeability variation. Water Resour. Res. 3 (2), 623–634. https://doi.org/10.1029/WR003i002p00623.

Freeze, R.A., Witherspoon, P.A., 1968. Theoretical analysis of regional ground water flow: 3. Quantitative Interpretations. Water Resour. Res. 4 (3), 581–590. https://doi.org/10.1029/WR004i003p00581.
Galsa, A., 1997. Modelling of groundwater flow along a section in the Great Hungarian Plain using hydraulic heads measured in wells (in Hungarian with English abstract). Magyar Geofizika 38 (4), 245–256.
Ge, S., Garven, G., 1989. Tectonically induced transient groundwater flow in foreland basin. In: Price, R.A. (Ed.), Origin and evolution of sedimentary basins and their energy and mineral resources. AGU,, Washington, D. C. pp. 145-157. Doi: 10.1029/GM048p0145, ISBN: 9780875904528.
Goldscheider, N., Mádl-Szőnyi, J., Erőss, A., Schill, E., 2010. Review: Thermal water resources in carbonate rock aquifers. Hydrogeol. J. 18 (6), 1303–1318. https://doi.org/10.1007/s10040-010-0611-3.
Han, W.S., Kim, K.-Y., Jung, N.-H., Park, E., Solomon, D.K., 2015. Transport of groundwater, heat and radiogenic He in topography-driven basins. Groundwater 53 (S1), 33–46. https://doi.org/10.1111/gwat.12266.
Harrison, W.J., Summa, L.L., 1991. Paleohydrology of the Gulf of Mexico Basin. Am. J. Sci. 291, 109–176. https://doi.org/10.2475/ajs.291.2.109.
Havril, T., Molson, J.W., Mádl-Szőnyi, J., 2016. Evolution of fluid flow and heat distribution over geological time scales at the margin of unconfined and confined carbonate sequences – a numerical investigation based on the Buda Thermal Karst analogue. Mar. Pet. Geol. 78, 738–749. https://doi.org/10.1016/j.marpetgeo.2016.10.001.
Hubbert, M.K., 1940. The theory of ground-water motion. Eos Trans. AGU 21 (2), 648. https://doi.org/10.1029/TR021i002p00648-1.
Horton, C.W., Rogers, F.T., 1945. Convection currents in a porous medium. J. Appl. Phys. 16 (6), 367–370. https://doi.org/10.1063/1.1707601.
Jiang, X.W., Wan, L., Wang, X.S., Ge, S., Liu, J., 2009. Effect of exponential decay in hydraulic conductivity with depth on regional groundwater flow. Geophys. Res. Lett. 36 (24), L24402. https://doi.org/10.1029/2009GL041251.
Jiang, X.W., Wang, X.S., Wan, L., 2010a. Semi – empirical equations for the systematic decrease in permeability with depth in porous and fractured media. Hydrogeol. J. 18 (4), 839–850. https://doi.org/10.1007/s10040-010-0575-3.
Jiang, X.W., Wan, L., Cardenas, M.B., Ge, S., Wang, X.S., 2010b. Simultaneous rejuvenation and aging of groundwater in basins due to depth-decaying hydraulic conductivity and porosity. Geophys. Res. Lett. 37 (5), L05403. https://doi.org/10.1029/2010GL042387.
Jiang, X.W., Wang, X.S., Wan, L., Ge, S., 2011. An analytical study on stagnation points in nested flow systems in basins with depth-decaying hydraulic conductivity. Water Resour. Res. 47 (1), W01512. https://doi.org/10.1029/2010WR009346.
Jiang, X.W., Wan, L., Wang, X.S., Wang, D., Wang, H., Wang, J.Z., Zhang, H., Zhang, Z.Y., Zhao, K.Y., 2018. A multi-method study of regional groundwater circulation in the Ordos Plateau, NW China. Hydrogeol. J. 26 (5), 1657–1668. https://doi.org/10.1007/s10040-018-1731-4.
Lapcevic, P.A., Novakowski, K.S., Sudickly, E., 1999. Groundwater flow and solute transport in fractured media. In: Delleur, J.W. (Ed.), Handbook of groundwater engineering. CRC, New York ISBN 978-3-540-64745-4.
Lapwood, E.R., 1948. Convection of a fluid in a porous medium. Math. Proc. CPS 44 (4), 508–521. https://doi.org/10.1017/S030500410002452X.
Lipsey, L., Pluymaekers, M., Goldberg, T., van Oversteeg, K., Ghazaryan, L., Cloetingh, S., van Wees, J.-D., 2016. Numerical modelling of thermal convection in the Luttelgeest carbonate platform, the Netherlands. Geothermics 64, 135–151. https://doi.org/10.1016/j.geothermics.2016.05.002.
Lopez, T., Antoine, R., Kerr, Y., Darrozes, J., Rabinowicz, M., Ramillien, G., Cazenave, A., Genthon, P., 2016. Subsurface hydrology of the lake chad basin from convection modelling and observations. Surv. Geophys. 37, 471–502. https://doi.org/10.1007/s10712-016-9363-5.
Lenkey, L., 1993. Study of thermal anomaly at Tiszakécske by numerical modelling of thermal convection (in Hungarian with English abstract). Magyar Geofizika 34 (1), 30–46.
Lenkey, L., Dövényi, P., Horváth, F., Cloetingh, S.A.P.L., 2002. Geothermics of the Pannonian Basin and its Bearing on the Neotectonics. Stephan Mueller Special Publication Series, pp. 29–40.
Lenkey, L., Raáb, D., Goetzl, G., Lapanje, A., Nádor, A., Rajver, D., Rotár-Szalkai, Á., Svasta, J., Zekiri, F., 2017. Acta Geod. Geophys. 52 (2), 161–182. https://doi.org/10.1007/s40328-017-0194-8.
Nield, D.A., Bejan, A., 2017. Convection in porous media, 5th. Springer Int. Pub. pp. 988, doi: 10.1007/978–3–319–49562–0, ISBN: 978–3–319–49561–3.
Mádl-Szőnyi, J., Tóth, Á., 2015. Basin-scale conceptual groundwater flow model for an unconfined and confined thick carbonate region. Hydrogeol. J. 23 (7), 1359–1380. https://doi.org/10.1007/s10040-015-1274-x.
Mádl-Szőnyi, J., Czauner, B., Iván, V., Tóth, Á., Simon, Sz, Erőss, A., Bodor, P., Havril, T., Boncz, L., Sőreg, V., 2017. Confined carbonates – Regional scale hydraulic interaction or isolation? Mar. Pet. Geol. (Accepted manuscript). https://doi.org/10.1016/j.marpetgeo.2017.06.006.
Mádl-Szőnyi, J., Szijártó, M., Tóth, Á., Iván, V., Galsa, A., Havril, T., Molson, J., 2018. Patterns and origin of heat anomalies in a carbonate system – joint interpretation of measured data and numerical simulations. Paper FP-250. Abstract Book. 45th International Association of Hydrogeology Congress, Daejeon, Korea 9–14 September.
Molson, J.W., Frind, E.O., 2017. HEATFLOW-SMOKER, Version 8.0 – density-dependent Flow and Advective-dispersive Transport of Thermal energy, Mass or Residence Time in Three-dimensional Porous or Directly-fractured Porous Media. Université Laval, Quebec, QC, Canada.
Oliver, J., 1986. Fluid expelled tectonically from orogenic belts: their role in hydrocarbon migration and other geologic phenomena. Geology 14 (2), 99–102. https://doi.org/10.1130/0091-7613(1986) 14<99:FETFOB>2.0.CO;2.
Pasquale, V., Chiozzi, P., Verdoya, M., 2013. Evidence for thermal convection in the deep carbonate aquifer of the eastern sector of the Po Plain, Italy. Tectonophysics 594, 1–12. https://doi.org/10.1016/j.tecto.2013.03.011.
Patankar, S.V., 1980. Numerical Heat Transfer and Fluid Flow. McGraw-Hill, New-York pp. 193, ISBN: 0-89116-522-3.
Person, M., Raffensperger, J.P., Ge, S., Garven, G., 1996. Basin-scale hydrogeologic modeling. Rev. Geophys. 34 (1), 61–87. https://doi.org/10.1029/95RG03286.
Rabinowicz, M., Boulègue, J., Genthon, P., 1998. Two- and three-dimensional modeling of hydrothermal convection in the sedimented Middle Valley segment, Juan de Fuca Ridge. J. Geophys. Res. 103 (B10), 24045–24065. https://doi.org/10.1029/98JB01484.
Raffensperger, J., Vlassopoulos, D., 1999. The potential for free and mixed convection in sedimentary basins. Hydrogeol. J. 7 (6), 505–520. https://doi.org/10.1007/s100400050224.
Robinson, N.I., Love, A.J., 2013. Hidden channels of groundwater flow in Tóthian drainage basins. Adv. Water Resour. 62, 71–78 Corrigendum (2017) 75, 118.
Scanlon, B.R., Mace, R.E., Barrett, M.E., Smith, B., 2003. Can we simulate regional groundwater flow in a karst system using equivalent porous media models? Case study, Barton Springs Edwards aquifer, USA. J. Hydrol. 276, 137–158. https://doi.org/10.1016/S0022-1694(03)00064-7.
Sharp, J.M., 1976. Momentum and energy balance equation for compacting sediment. Mathemat. Geosci. 8 (3), 305–322. https://doi.org/10.1007/BF01029275.
Shojae Ghias, M., Therrien, R., Molson, J., Lemieux, J.M., 2017. Controls on permafrost thaw in a coupled groundwater-flow and heat-transport system: Iqaluit Airport, Nunavut. Canada. Hydrogeol. J. 25 (3), 657–673. https://doi.org/10.1007/s10040-016-1515-7.
Simmons, C.T., Narayan, K.A., Wooding, R.A., 1999. On a test case for density-dependent groundwater flow and solute transport models: the Salt Lake problem. Water Resour. Res. 35 (12), 3607–3620. https://doi.org/10.1029/1999WR900254.
Smith, L., Chapman, D.S., 1983. On the thermal effects of groundwater flow: 1. Regional scale systems. J. Geophys. Res. 88 (B1), 593–608. https://doi.org/10.1029/JB088iB01p00593.
Straus, J.M., Schubert, G., 1977. Thermal convection of water in a porous medium: effects of temperature- and pressure-dependent thermodynamic and transport properties. J. Geophys. Res. 82 (2), 325–333. https://doi.org/10.1029/JB082i002p00325.
Tóth, J., 1962. A theory of groundwater motion in small drainage basins in central Alberta. Canada. J. Geophys. Res. 67 (22), 4375–4387. https://doi.org/10.1029/JZ067i011p04375.
Tóth, J., 1963. A theoretical analysis of groundwater flow in small drainage basins. J. Geophys. Res. 68 (16), 4795–4812. https://doi.org/10.1029/JZ068i016p04795.
Tóth, J., 1988. Ground water and hydrocarbon migration, in Hydrogeology: Geology of North America. Geol. Soc. Am. Boulder, Colo., pp. 485–502.
Tóth, J., 1999. Groundwater as a geologic agent: An overview of the causes, processes, and manifestations. Hydrogeol. J. 7 (1), 1–14. https://doi.org/10.1007/s100400050176.
Tóth, J., 2009. Gravitational systems of groundwater flow: theory, evaluation, utilization. Cambridge University Press, United Kingdom pp. 297, ISBN: 978–0–521–88638–3.
Tóth, J., Almási, I., 2001. Interpretation of observed fluid potential patterns in a deep sedimentary basin under tectonic compression: Hungarian Great Plain. Pannonian Basin, Geofluids 1, 11–36. https://doi.org/10.1046/j.1468-8123.2001.11004.x.
Turcotte, D.L., Schubert, G., 2002. Geodynamics. Cambridge University Press pp. 456, ISBN: 0–521–66186–2.
van Dam, R.L., Simmons, C.T., Dydman, D.W., Wood, W.W., 2009. Natural free convection in porous media: first field documentation in groundwater. Geophys. Res. Lett. 36, L11403. https://doi.org/10.1029/2008GL036906.
Voss, C.I., Souza, W.R., 1987. Variable density flow and solute transport simulation of regional aquifers containing a narrow freshwater-saltwater transition zone. Water Resour. Res. 23 (10), 1851–1866. https://doi.org/10.1029/WR023i010p01851.
Voss, C.I., Simmons, C.T., Robinson, N.I., 2010. Three-dimensional benchmark for variable-density flow and transport simulation: matching semi-analytic stability modes for steady unstable convection in an inclined porous box. Hydrogeol. J. 18 (1), 5–23. https://doi.org/10.1007/s10040-009-0556-6.
Wang, X.S., Jiang, X.W., Wan, L., Ge, S., Li, H., 2011. A new analytical solution of topography-driven flow in a drainage basin with depth-dependent anisotropy of permeability. Water Resour. Res. 47 (9), W09603. https://doi.org/10.1029/2011WR010507.
Weast, R.C., 1980. CRC Handbook of Chemistry and Physics, 60th ed. CRC Press, Cleveland, Ohio, pp. 2454.
Winter, T.C., Pfannkuch, H.O., 1984. Effect of anisotropy and groundwater system geometry on seepage through lakebeds. J. Hydrol. 75 (1-4), 239–253. https://doi.org/10.1016/0022-1694(84)90052-0.
Yang, J., Large, R.R., Bull, S.W., 2004. Factors controlling free thermal convection in faults in sedimentary basins: implications for the formation of zinc-lead mineral deposits. Geofluids 4 (3), 237–247. https://doi.org/10.1111/j.1468-8123.2004.00084.x.
Yang, J., Large, R.R., Bull, S., 2006. Basin-scale numerical modeling to test the role of buoyancy-driven fluid flow and heat transfer in the formation of stratiform Zn-Pb-Ag Deposits in the Northern Mount Isa Basin. Econ. Geol. 101 (6), 1275–1292. https://doi.org/10.2113/gsecongeo.101.6.1275.
Yang, J.W., Feng, Z.H., Luo, X.R., Chen, Y.R., 2010. Numerically quantifying the relative importance of topography and buoyancy in driving groundwater flow. Sci. China Ser. D-Earth Sci. 53 (1), 64–71. https://doi.org/10.1007/s11430-009-0185-x.
Zhang, Y., Person, M., Gable, C.W., 2007. Representative hydraulic conductivity of hydrogeologic units: Insights from an experimental stratigraphy. J. Hydrol. 339 (1–2), 65–78. https://doi.org/10.1016/j.jhydrol.2007.03.007.
Zhang, Z.Y., Jiang, X.W., Wang, X.S., Wan, L., Wang, J.Z., 2018. A numerical study on the occurrence of flowing wells in the discharge area of basins due to the upward hydraulic gradient induced wellbore flow. Hydrogeol. Process. 48 (12), W12502. https://doi.org/10.1002/hyp.11623.
Zimmermann, W.B.J., 2006. Multiphysics modeling with finite element methods. World Scientific Publishing Company Singapore pp. 422, ISBN: 981–256–843–3.